Journal of Marine Science and Engineering

MDPI

Article

Numerical Simulation on Hybrid Lifting Operation of Polymetallic Nodules and Rare-Earth Elements-Rich Mud by Air-Lift Pump in Deep Sea around Minamitorishima Island

Yoshiyuki Shimizu [1,2,3,*], Masatoshi Sugihara [2], Koichiro Fujinaga [3,4], Kentaro Nakamura [3,4] and Yasuhiro Kato [4,5]

[1] ShimizuLab, Itasca JAPAN, Shizuoka 420-0862, Japan
[2] Former, School of Marine Science & Technology, Tokai University, Shizuoka 424-8610, Japan; diamachine@gmail.com
[3] Frontier Research Center for Energy and Resources (FRCER), School of Engineering, The University of Tokyo, Tokyo 113-8656, Japan; koichiro.fujinaga@p.chibakoudai.jp (K.F.); kentaron@sys.t.u-tokyo.ac.jp (K.N.)
[4] Ocean Resources Research Center for Next Generation (ORCeNG), Chiba Institute of Technology, Narashino 275-0016, Japan; ykato@sys.t.u-tokyo.ac.jp
[5] Department of Systems Innovation, School of Engineering, The University of Tokyo, Tokyo 113-8656, Japan
* Correspondence: yoshi@itasca.jp

Abstract: Polymetallic nodules and REE-rich mud under the seabed of 5500–5700 m water depth around Minamitorishima island are promising and attractive for exploration and development. Following our previous research, numerical analysis was used to investigate the unsteady flow characteristics and the lifting performance of a commercial production system using an air-lift pump for hybrid lifting, lifting both polymetallic nodules and REE-rich mud. Gas–liquid–solid three-phase flow and gas–liquid two-phase flow in the system were analyzed using the one-dimensional drift–flux model. First, the reliability of the schemes and program was verified by comparing the numerical results with the experimental ones. Next, numerical simulations were conducted, in which the model's dimensions were related to a commercial production system operated in the deep sea around Minamitorishima island, and the conditions fit the expected production rate. The results revealed the unsteady flow characteristics under the operations, such as start-up, shut-down, feed of polymetallic nodules and REE-rich mud, and those associated with disturbances, such as feed rate fluctuations. We demonstrate that the program and the schemes can simulate the unsteady flow characteristics and the lifting performance of a commercial production system with an air-lift pump well, and they can derive useful information and know-how in advance for the safe and continuous operation of the system.

Keywords: numerical simulation; hybrid lifting operation; polymetallic nodules; REE-rich mud; air-lift pump; Minamitorishima island; unsteady flow characteristics; one-dimensional drift–flux model

Academic Editor: Antoni Calafat

Received: 8 January 2025
Revised: 27 January 2025
Accepted: 29 January 2025
Published: 31 January 2025

Citation: Shimizu, Y.; Sugihara, M.; Fujinaga, K.; Nakamura, K.; Kato, Y. Numerical Simulation on Hybrid Lifting Operation of Polymetallic Nodules and Rare-Earth Elements-Rich Mud by Air-Lift Pump in Deep Sea around Minamitorishima Island. *J. Mar. Sci. Eng.* **2025**, *13*, 267. https://doi.org/10.3390/jmse13020267

1. Introduction

Polymetallic nodules and Rare-earth elements-rich mud (hereafter, "REE-rich mud"), which exist under the seabed of 5500–5700 m water depth around Minamitorishima island, Japan [1–3], are promising and attractive because of their volume and composition, comprising materials such as manganese, nickel, cobalt, and REEs. The exploration and development of these mineral resources are urgent challenges due to

the recent paradigm shift from fossil fuels to renewable energy sources through lower-carbon technologies.

Following our previous study [4], a production system using an air-lift pump (Figure 1, left) is applied for lifting polymetallic nodules and REE-rich mud from the deep sea in this study. The system with an air-lift pump consists of a mining ship, in which an air compressor and a gas–liquid–solid separator are set up; a lifting pipe; an air pipe; and a mining unit including an excavator, a collector, and a classifier on the seabed. Note that the gas–liquid–solid separator is used for post-processing to classify the lifted air, seawater, or mud water with REE-rich mud and polymetallic nodules. It is a hydraulic transport system [5] that continuously transports polymetallic nodules and REE-rich mud by the use of upward seawater flow from the seabed to the sea surface through a lifting pipe. The upward flow is created by a hydrostatic pressure difference between the inside and outside of the lifting pipe, while air pressurized by the air compressor is injected through an air pipe near the middle of the lifting pipe via an air injection point. The flow in the lifting pipe is a multi-phase. For instance, in the case of lifting both polymetallic nodules and REE-rich mud (hereafter, "hybrid lifting"), it is a mixture of seawater, REE-rich mud, and polymetallic nodules, i.e., liquid (mud water)–solid (polymetallic nodules) two-phase flow below the air injection point, and gas (air)–liquid (mud water)–solid (polymetallic nodules) three-phase flow above the air injection point.

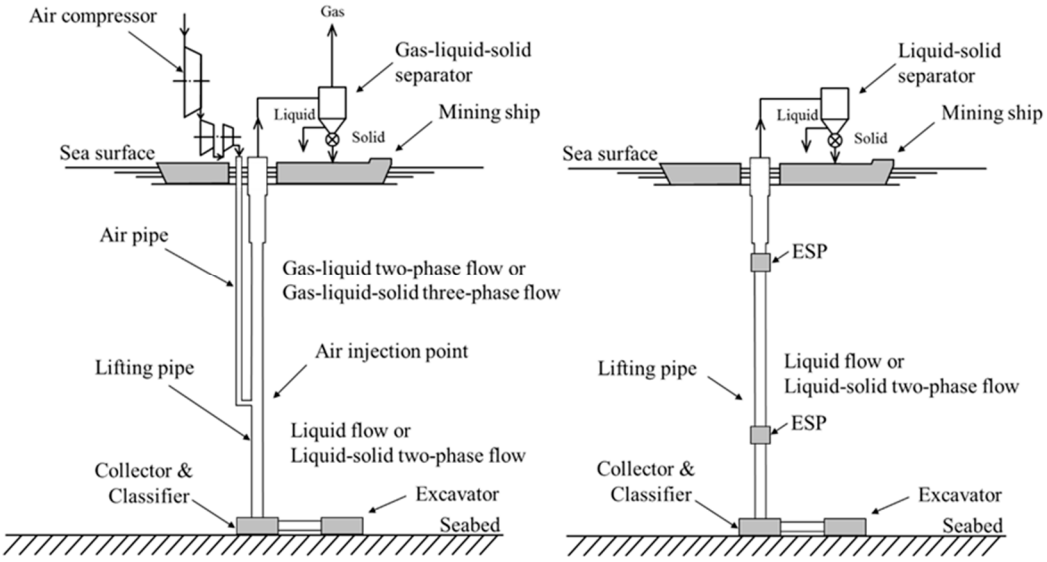

Figure 1. Deep sea production systems with an air-lift pump (left) and electric submersible pumps (ESPs) (right) after Shimizu et al. (2024) [4].

The system with an air-lift pump is one of the hydraulic dredging systems. The other is with electric submersible pumps (ESPs) set up in series on the lifting pipe (Figure 1, right). The advantage of the system with an air-lift pump is that it is maintenance-free, as there are no specific mechanical devices underwater as there are with ESPs. Therefore, the system with an air-lift pump is more likely to be adopted for deep sea operations (5000–6000 m water depth) [6,7] than that with ESPs [8]. Also, the classification and mineral processing of the lifted polymetallic nodules on the mining ship is relatively easy under a system with an air-lift pump because of less degradation of the nodules compared with the system with ESPs. However, the efficiency is, in most cases, lower than that of ESPs. One scheme for overcoming this drawback is specifying a back pressure at the exit of the lifting pipe. By returning the pressurized air to the inlet of the air compressor, the power requirements decrease. In addition, the back pressure keeps the mixture velocity near the

sea surface at a lower level, consequently reducing the erosion inside the lifting pipe and the gas–liquid–solid separator.

In Japan, several projects have been carried out to develop polymetallic nodules around Hawaii in the deep sea [9–13], and others have been conducted for the development of the REE-rich mud around Minamitorishima island [14–16] under cooperation with the government, academia, and industry. In studies on the system with an air-lift pump, Hatakeyama [17] and Hatakeyama et al. [18] extended the one-dimensional drift-flux model to the gas–liquid–solid three-phase flow, and then applied it for simulations of lifting polymetallic nodules. The authors have conducted a numerical study on a system with an air-lift pump for mining polymetallic nodules and REE-rich mud from the deep sea to clarify the lifting performances and examine the flow characteristics when lifting REE-rich mud, polymetallic nodules, and both, i.e., hybrid lifting [4]. However, the dimensions of simulation models were smaller than those for a commercial production system. Also, the validation of the numerical schemes and the program was conducted using data with steady flows, not unsteady flows. Consequently, the unsteady flow characteristics and the lifting performance on a commercial production-scaled system with an air-lift pump have not been examined yet.

Based on our previous research [4], this study examines the unsteady flow characteristics and the lifting performance of a commercial production system using an air-lift pump for hybrid lifting, lifting both polymetallic nodules and REE-rich mud from the 5500–5700 m deep sea around Minamitorishima island, to derive useful information and find an appropriate method for operating the system safely and continuously. Gas–liquid–solid three-phase flow and gas–liquid two-phase flow in the system are analyzed using the one-dimensional drift–flux model, which was also adopted in the previous study. The air flow analysis in the air pipe is newly added, and coupled with the flow in the lifting pipe. First, the calculation results related to the unsteady flow characteristics, i.e., time transient results are compared with the published experimental ones to validate the numerical schemes and the program. Next, numerical simulations are conducted, in which the model's dimensions are related to a commercial production system operated in the deep sea around Minamitorishima island, and the conditions fit the expected production rate.

2. Method: Numerical Scheme and Program

The one-dimensional drift flux model [17,19,20] is adopted as the numerical scheme in the study, which is the same as that in our previous study [4], and described briefly here.

The momentum and mass conservation equations of the gas–liquid–solid three-phase mixture, and the mass conservation equation of gas and solid each phase are shown by Equations (1)–(3). Note that the subscripts of G, L, S, and M represent gas, liquid, solid, and gas–liquid–solid three-phase mixture (hereafter, "mixture"), respectively.

$$\begin{aligned}&\frac{\partial}{\partial t}\left(\rho_{\mathrm{M}}V_{\mathrm{M}}\right)+\frac{\partial}{\partial z}\left(\rho_{\mathrm{M}}V_{\mathrm{M}}{}^{2}\right)\\&=-\frac{\partial P_{\mathrm{M}}}{\partial z}-\frac{4\tau_{\mathrm{W}}}{D}+\rho_{\mathrm{M}}g-\frac{\partial\left(\rho_{\mathrm{G}}F_{\mathrm{G}}W_{\mathrm{G}}{}^{2}\right)}{\partial z}-\frac{\partial\left(\rho_{\mathrm{L}}F_{\mathrm{L}}W_{\mathrm{L}}{}^{2}\right)}{\partial z}-\frac{\partial\left(\rho_{\mathrm{S}}F_{\mathrm{S}}W_{\mathrm{S}}{}^{2}\right)}{\partial z}\end{aligned}\tag{1}$$

$$\frac{\partial\rho_{\mathrm{M}}}{\partial t}+\frac{\partial}{\partial z}\left(\rho_{\mathrm{M}}V_{\mathrm{M}}\right)=\Gamma_{\mathrm{G}}+\Gamma_{\mathrm{L}}+\Gamma_{\mathrm{S}}\tag{2}$$

$$\frac{\partial}{\partial t}\left(F_k\rho_k\right)+\frac{\partial}{\partial z}\left(F_k\rho_kV_k\right)=\Gamma_k\qquad\left(k=\mathrm{G,S}\right)\tag{3}$$

V_M and ρ_M in Equations (1) and (2) are defined as center-of-mass velocity and density of the mixture, and given by (4) and (5), respectively.

$$V_{\mathrm{M}} = \left(F_{\mathrm{G}}\rho_{\mathrm{G}}V_{\mathrm{G}} + F_{\mathrm{L}}\rho_{\mathrm{L}}V_{\mathrm{L}} + F_{\mathrm{S}}\rho_{\mathrm{S}}V_{\mathrm{S}}\right)/\rho_{\mathrm{M}} \tag{4}$$

$$\rho_{\mathrm{M}} = F_{\mathrm{G}}\rho_{\mathrm{G}} + F_{\mathrm{L}}\rho_{\mathrm{L}} + F_{\mathrm{S}}\rho_{\mathrm{S}} \tag{5}$$

where

p_M: pressure of mixture [Pa(G)];

$F_k(k = G, L, S)$: volume fraction of the k-phase [-];

$V_k(k = G, L, S)$: velocities of the k-phase [m/s];

$W_k = V_k - V_{\mathrm{M}}(k = \mathrm{G, L, S})$: velocities of the k-phase relative to the center-of-mass velocity of mixture [m/s];

$\rho_k(k = \mathrm{G, L, S})$: density of the k-phase [kg/m^3];

$\Gamma_k(k = \mathrm{G, L, S})$: source term of the k-phase per unit volume [kg/(m^3· s)];

τ_{W}: shear stress by pipe friction [Pa];

D: pipe diameter [m];

g: gravitational acceleration [m/s^2];

t: time [s];

z: coordinate in the axial direction of the lifting pipe, from bottom to top [m].

Using these equations along with the fact that $F_{\mathrm{G}} + F_{\mathrm{L}} + F_{\mathrm{S}} = 1$, V_{M}, P_{M}, and $F_k(k = \mathrm{G, L, S})$, also the volume concentration of mud within the liquid-phase $C_{\mathrm{X}}(\equiv F_{\mathrm{X}}/F_{\mathrm{L}})$, are evaluated as functions of time and one-dimensional space in each section along the lifting pipe.

Velocities of the gas- and solid-phase relative to the center-of-mass velocity of the mixture $W_k(k = \mathrm{G, S})$ are derived by the drift velocities of the gas- and solid-phase $V_{k\_\mathrm{dfj}}(k = \mathrm{G, S})$, i.e., velocities of the gas- and solid-phase relative to mixture flux, defined by Equation (6). Parameters in Equation (6) of the gas-phase are summarized in Table 1, and those of the solid-phase are shown in Table 2.

$$V_{k\_\mathrm{dfj}} = \left(C_{\mathrm{k0}} - 1\right)J_{\mathrm{M}} + V_{kj} \qquad \left(k = \mathrm{G, S}\right) \tag{6}$$

Table 1. Parameters to calculate drift velocities of gas-phase [20].

Flow Regime	F_{G} Range	V_{Gj}	C_{G0}
Bubble Flow	$F_{\mathrm{G}} \le 0.2$	$\sqrt{2}\left(\frac{\sigma g \Delta\rho}{\rho_{\mathrm{L}}^{\ 2}}\right)^{1/4}\left(1 - F_{\mathrm{G}}\right)^{1.5}$	$1.2 - 0.2\sqrt{\rho_{\mathrm{G}}/\rho_{\mathrm{L}}}$
Slug Flow	$0.3 \le F_{\mathrm{G}} \le 0.7$	$0.35\left(\frac{g\Delta\rho D_{\mathrm{P}}}{\rho_{\mathrm{L}}}\right)^{1/2}$	$1.2 - 0.2\sqrt{\rho_G/\rho_L}$
Annular Flow	$F_{\mathrm{G}} \ge 0.8$	$\frac{1 - F_{\mathrm{G}}}{F_{\mathrm{G}} + 4\sqrt{\rho_{\mathrm{G}}/\rho_{\mathrm{L}}}}\left(\frac{\Delta\rho g D_{\mathrm{P}}\left(1 - F_{\mathrm{G}}\right.}{0.015\rho_{\mathrm{L}}}\right.$	$1 + \frac{1 - F_{\mathrm{G}}}{F_{\mathrm{G}} + 4\sqrt{\rho_{\mathrm{G}}/\rho_{\mathrm{L}}}}$

Note that V_{Gj} is specified for each flow regime, i.e., bubble flow, slug flow, or annular flow, which is classified by the volume fraction of the gas-phase F_{G}. Also, V_{Gj} is approximated linearly in the range of 0.2 to 0.3, and 0.7 to 0.8 of the volume fraction.

Table 2. Parameters to calculate drift velocities of solid-phase [21,22].

V_{Sj}	C_{S0}
$-V_{\mathrm{SS}}\varepsilon^{1.35}$	$1.2V_{\mathrm{L}}/J_{\mathrm{M}}$

Note that V_{Sj} is calculated by the hindered settling velocity of the particle system, expressed by a voidage function [21]. V_{SS}: terminal velocity; ε: porosity $(F_{\mathrm{L}}/(F_{\mathrm{L}}+F_{\mathrm{S}}))$.

Shear stress by pipe friction τ_{W} in Equation (1), which is the pressure drop of mixture ΔP_{M}, is evaluated using Akagawa's formula given by Equation (7) [23–26].

$$\Delta P_{\mathrm{M}} = \Delta P_{\mathrm{L}}\left(1-F_{\mathrm{G}}\right)^{-Z_{\mathrm{a}}} \tag{7}$$

where Z_{a} is the parameter in Akagawa's formula, and ΔP_{L} represents pressure drop by the flowing liquid-phase with liquid flux, given by Equation (8).

$$\Delta P_{\mathrm{L}} = \lambda\frac{\rho_{\mathrm{L}}}{2}J_{\mathrm{L}}{}^{2}\frac{L}{D} \tag{8}$$

In the case of mining polymetallic nodules, liquid plus solid flux $J_{\mathrm{L}}+J_{\mathrm{S}}$ is used instead of J_{L} in Equation (8) under the assumption that the solid particles migrate with liquid flow. Note that an additional pressure drop should be considered in Equation (8) for particle–liquid two-phase flow if the lifting pipe is placed horizontally or inclined.

In the case of mining REE-rich mud, mud water (a mixture of REE-rich mud and seawater) shows the flow characteristics of a pseudo-plastic fluid, as shown by Equation (9). The parameters in Equation (9), i.e., the flow consistency index $K[\mathrm{Pa}\cdot\mathrm{s}^{\mathrm{n}}]$ and the flow behavior index $n\,[-]$, depend on the volume concentration of mud within the liquid-phase $C_{\mathrm{X}}(=F_{\mathrm{X}}/F_{\mathrm{L}})$. Empirical equations are summarized in Table 3 [4]. The pipe friction factor λ in Equation (8) is evaluated using these parameters as a function of C_{X} [27–30]. The formulas by Kemblowski and Kolodziejski [31] are used to calculate the factor under turbulent flow for a smooth circular pipe, and those by Masuyama and Hatakeyama [28] for a rough circular pipe.

$$\tau = K\dot{\gamma}^{n} \tag{9}$$

Table 3. Empirical equations for flow consistency index K and flow behavior index n [4].

	Flow Consistency Index K	**Flow Behavior Index** n	
Original Mud Water	$\mu_0\left(8.91\times10^{6}C_{\mathrm{X}}{}^{2.83}+1.0\right)$	$-1.85C_{\mathrm{X}}{}^{0.282}+1.0$	$\left(0\le C_{\mathrm{X}}\le 0.05\right)$
		$-0.639C_{\mathrm{X}}+0.237$	$\left(0.05\le C_{\mathrm{X}}\le 0.10\right)$
UF After Hydrocyclone	$\mu_0\left(6.76\times10^{5}C_{\mathrm{X}}{}^{2.56}+1.0\right)$	$-1.09C_{\mathrm{X}}{}^{0.175}+1.0$	

μ_0: viscosity of seawater; UF: underflow mud water, which contains high concentrations of REEs.

The finite volume method is adopted to discretize Equations (1)–(3) and integrate over the control volume. The pressure and volume fractions of each phase are defined at the center of each control volume, and the velocities at the boundary between two control volumes. Additionally, the analysis for the air pipe (hereafter, "the air pipe analysis") is added after our previous study [4] and then coupled with the analysis for the lifting pipe (hereafter, "the lifting pipe analysis").

Figure 2 shows the flows of the program. The analytical time goes forward with the time-step Δt, i.e., an unsteady analysis. The air pipe analysis and the lifting pipe analysis are executed in turns. In the lifting pipe analysis, V_{M}, P_{M}, and $F_k(k=\mathrm{G},\mathrm{L},\mathrm{S})$ are calculated in each calculation unit. The iteration procedure is repeated until the errors in each calculation unit decrease within the criteria at each analytical time. In the air pipe analysis,

a mass flow rate of air is specified as a velocity boundary at the inlet of the air pipe. The pressure at the air injection point calculated in the lifting pipe analysis is used as a pressure boundary at the outlet of the air pipe. The calculated mass flow rate of air at the outlet of the air pipe is passed to the lifting pipe analysis and added as a source term of the gas-phase Γ_G in Equations (2) and (3) at the element related to the air injection point; the air is injected into the lifting pipe through the air pipe via the air injection point. The Semi-Implicit Method for Pressure Linked Equations (SIMPLE) scheme is used to solve V_M and P_M in the lifting pipe analysis, also V_G and P_G in the air pipe analysis. The first-order upwind difference scheme is adopted when discretizing convective terms in the momentum and mass conservation equations.

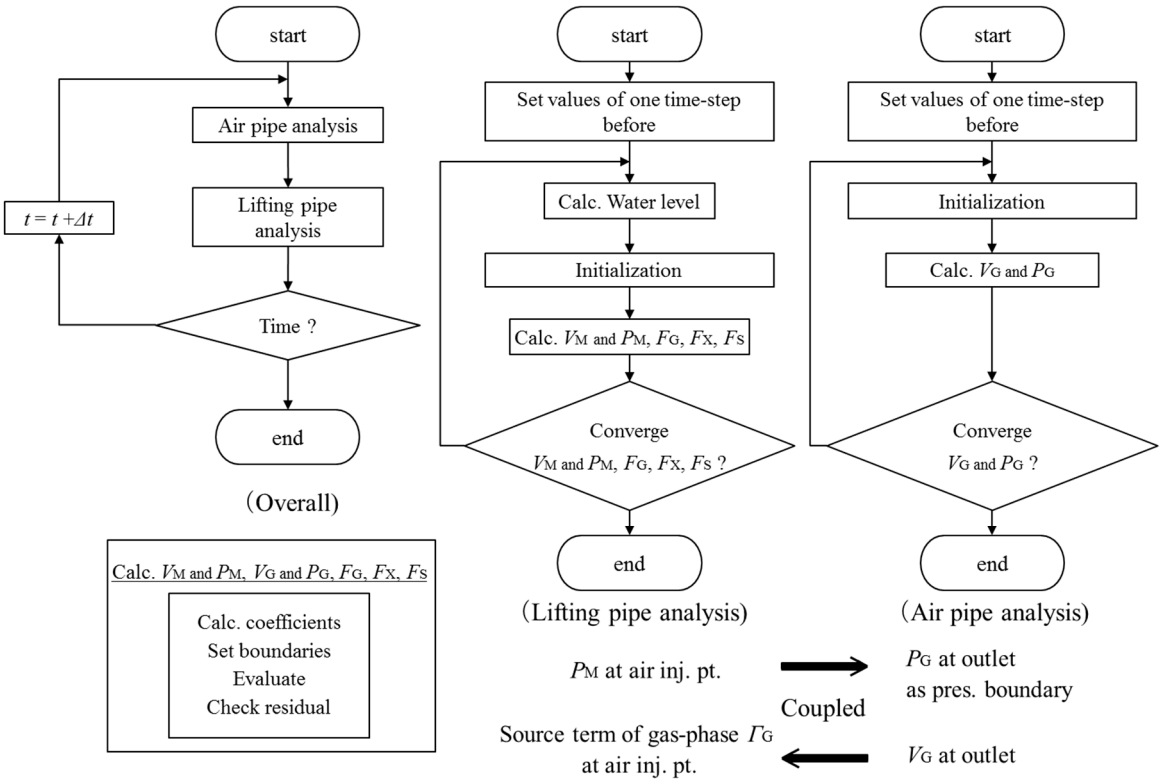

Figure 2. Flows of the program: overall (left), lifting pipe analysis (middle), and air pipe analysis (right).

3. Verification on Unsteady Flow Characteristics, Comparisons with Experimental Studies

3.1. Numerical Model

Figure 3 shows a numerical model, and the dimensions and the boundary conditions are based on related previous experiments [12,13]. The lifting pipe and the air pipe are placed vertically. The dimensions of the pipes are shown in Table 4. In total, 200 and 184 elements are created by dividing the lifting pipe and the air pipe into equal lengths of 1.063 and 1.0 m, respectively. The air flow rate is 15 or 25 Nm^3/min. A velocity corresponding to the air flow rate is specified at the inlet of the air pipe. The pressure at the air injection point by the lifting pipe analysis is specified at the outlet of the air pipe as a pressure boundary. The air is input into the lifting pipe through the air pipe at 184 m water depth. A pressure of zero Pa(G) is specified at the top of the lifting pipe. The hydrostatic pressure at a water depth of 200 m is specified at the bottom. The physical properties of air, water, and gravel used in the analysis are shown in Table 5. The density of air is calculated by Equation (10). The drag coefficient of gravel is calculated using the method of Sato et al.

[32,33]. The time-step of the analysis is 0.2 s, and unsteady flow data, i.e., time transient data are recorded every 0.2 s.

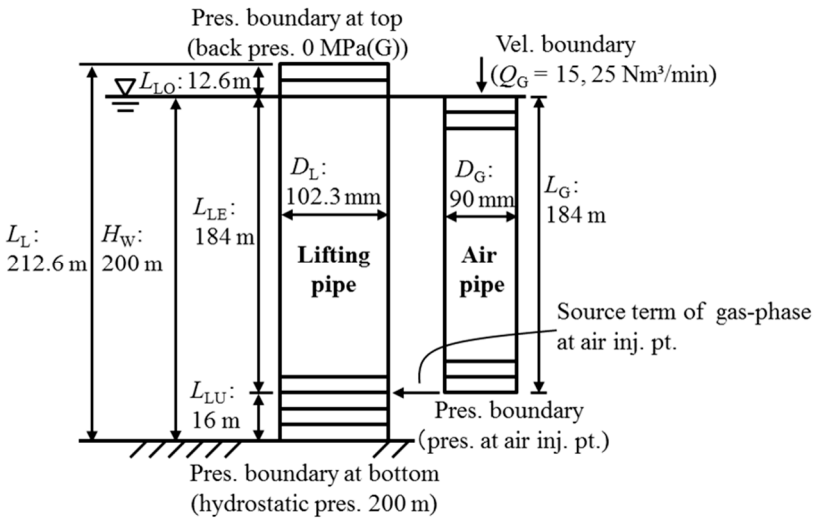

Figure 3. A numerical model and boundary conditions for verification, lifting pipe (left), and air pipe (right).

Table 4. Pipe dimensions of the numerical model for verification.

		Lifting Pipe				Air Pipe	
H_W	L_L	L_{LO}	L_{LE}	L_{LU}	D_L	L_G	D_G
[m]	[m]	[m]	[m]	[m]	[mm]	[m]	[mm]
200	212.6	12.6	184	16	102.3	184	90

Table 5. Physical properties, air, water, and gravel for verification.

Material	Density	Viscosity	Surface Tension	Molecular Mass	Particle Dia. D_P	Drag Coef. C_D
	[kg/m³]	[Pa·s]	[N/m]	[kg/mol]	[mm]	[-]
Air	Equation (10)	1.76×10^{-5}	7.4×10^{-2}	2.88×10^{-2}	-	-
Water	1.0×10^{3}	1.31×10^{-3}	-	-	-	-
Gravel	2.65×10^{3}	-	-	-	15	1.17

$$\rho_G = \frac{M}{R}\frac{(P_M + P_{at.})}{(T + 273.15)} \quad (10)$$

where T: temperature, 10.0 [degrees (Celsius)]; $P_{at.}$: atmospheric pressure, 1.01×10^5 [Pa]; M: molecular weight, air: 2.88×10^{-2} [kg/mol]; R: gas constant, 8.3145 [J/(mol·K)].

3.2. Results and Discussion: Unsteady Flow Characteristics of Lifting Water

Figure 4 shows the unsteady flow characteristics of an air-lift pump; the transient response of air flow rate (the first) and water flow rate (the second) at a start-up stage, i.e., beginning the input of air into the air pipe from the inlet at an air flow rate of 15 Nm³/min. The graphs in the left panel show the experimental result from the previous studies [12], and the ones in the right panel show the calculated one. Note that in the first graphs of both panels, the solid line: air flow rate at the top of the lifting pipe, the dashed line: at the air injection point (only right panel), and the dashed–dotted line: at the inlet of the air pipe, i.e., specified air flow rate. In the second graph of both panels, the solid line: water flow rate at the top of the lifting pipe, and the dashed line: at the bottom (190 m water

depth in case of experimental result). At the start-up stage of the experiment, the following characteristics are revealed: It takes a few minutes to begin lifting water after the air blow starts because the water initially in the air pipe is discharged, and the water level rises in the lifting pipe. When there is enough air in the lifting pipe to lift water, water is sucked into the lifting pipe from the bottom. At 40 s after beginning the input of air, water is discharged from the top of the lifting pipe. The water flow rate at the top temporarily increases at first because of discharging plugged water, which is initially preserved in the lifting pipe. The water flow rate is about 2.94 times that at the steady state (3.00 times in calculation). Subsequently, the air flow rate at the top increases with the discharge of the substantial amount of air used for displacing the plug of water. This air flow rate is 1.88 times that at the steady state (7.02 times in calculation). The system then enters a steady state. Although the calculated result shows a distinct peak in the air flow rate at the top of the lifting pipe compared with the experimental one, the calculated result substantially agrees with the experimental one.

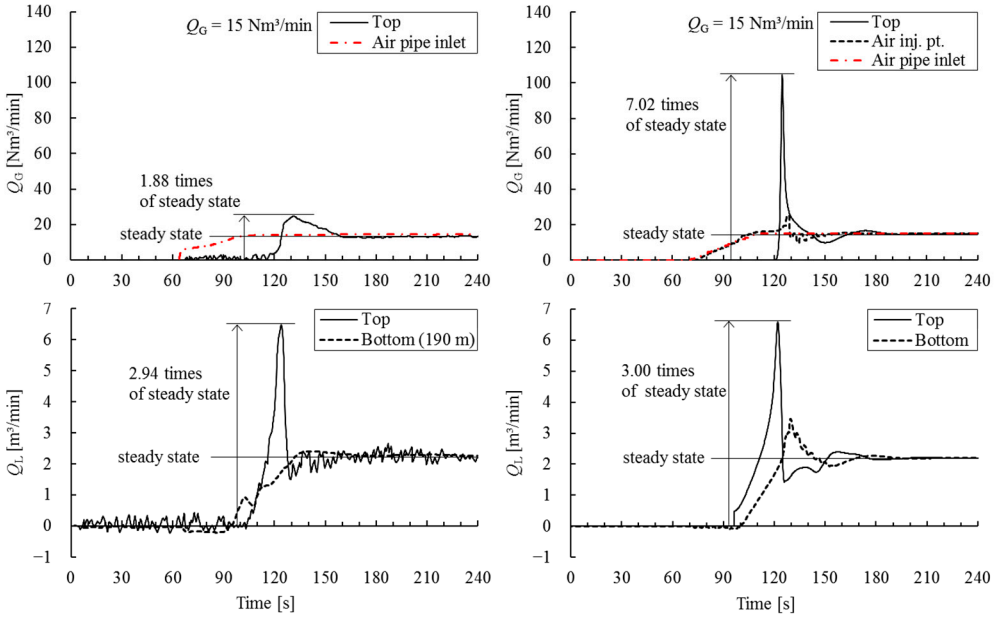

Figure 4. Unsteady flow characteristics of an air-lift pump at start-up, i.e., beginning the input of air; the experimental result from the previous studies [12] (left panel) versus the calculated one (right panel).

Figure 5 shows the unsteady flow characteristics of an air-lift pump; the transient response of air flow rate (the first) and water flow rate (the second) at a shut-down stage, i.e., stopping the input of air into the air pipe at 15 Nm³/min. The graphs in the left panel show the experimental result from the previous study [12], and the ones in the right panel show the calculated one. Water flow in the lifting pipe continues for a while at the shut-down stage, even after the input of air has stopped into the air pipe. When the air flow rate decreases, the water flow rate at the bottom of the lifting pipe increases temporarily, and then it gradually decreases. The water flow in the lifting pipe stops about 40 s after the air flow stops. The calculated result agrees sufficiently with the experimental one.

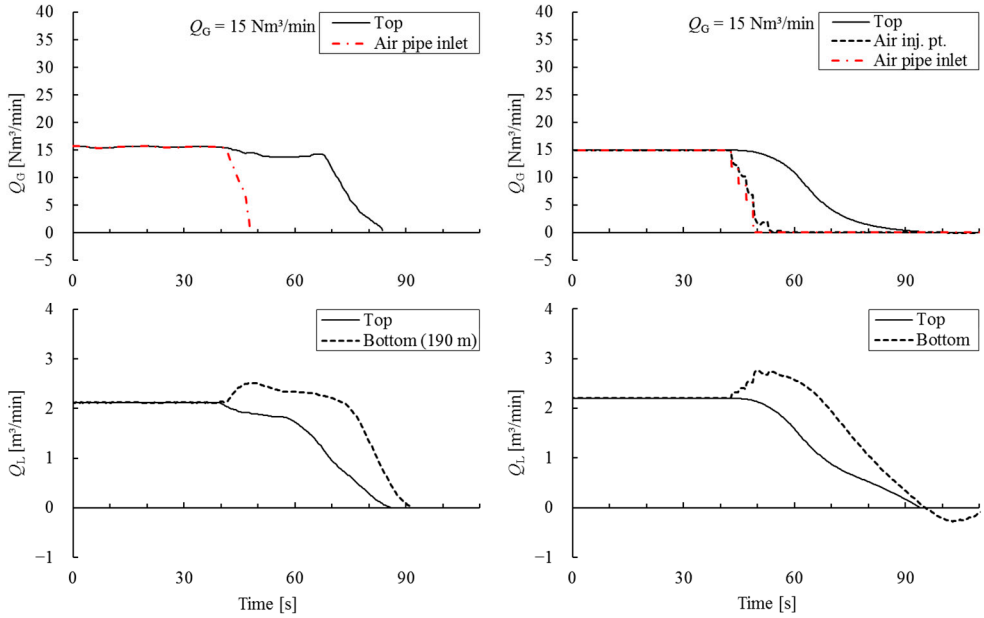

Figure 5. Unsteady flow characteristics of an air-lift pump at shut-down, i.e., stopping the input of air, the experimental result from the previous study [12] (left panel) versus the calculated one (right panel). Note that the solid, dashed, and dashed–dotted lines in each graph represent the same items shown in Figure 4.

3.3. Results and Discussion: Unsteady Flow Characteristics of Lifting Gravel

Figure 6 shows the unsteady flow characteristics of an air-lift pump; the transient response of air flow rate (the first), slurry (water plus gravel) flow rate (the second), mass flow rate (the third), and volume fraction of gravel within the slurry (the fourth) when changing air flow rate in a step fashion while the system is at a steady state, i.e., at 15 Nm³/min air flow rate, and 5% volume fraction of gravel. The graphs in the left panel show the experimental result from the previous studies [12], and the ones in the right panel show the calculated one. Note that in the first graphs of both panels, the solid line: air flow rate at the top, the dashed line: at the air injection point (only right panel), and the dashed–dotted line: at the inlet of the air pipe, i.e., specified air flow rate. In the second graph of both panels, the solid line: slurry (water plus gravel) flow rate at the top, and the dashed line: at the bottom (190 m water depth in case of experimental result). In the third graph of both panels, the solid line: flow rate of gravel at the top, and the dashed line: at the bottom (only right panel). In the fourth graph of both panels, the solid line: volume fraction of gravel within the slurry (water plus gravel) at the top (only right panel), and the dashed line: at the bottom. When the air flow rate suddenly increases or decreases from a steady state, there are momentary changes at the various points in the systems because of the loss of equilibrium in the lifting pipe. When the air flow rate suddenly increases, the slurry flow rate at the bottom decreases, and that at the top increases temporarily. On the other hand, when the air flow rate suddenly decreases, the slurry flow rate at the bottom increases, and that at the top decreases temporarily. After that, the system reaches a steady state. This happens because of a temporary loss of equilibrium between the power and the load in the air-lift pump. The calculated result also reveals the temporary loss of equilibrium, i.e., the slurry flow rate changes temporally at the top and the bottom, when the air flow rate suddenly decreases or increases, and follows the transient response well.

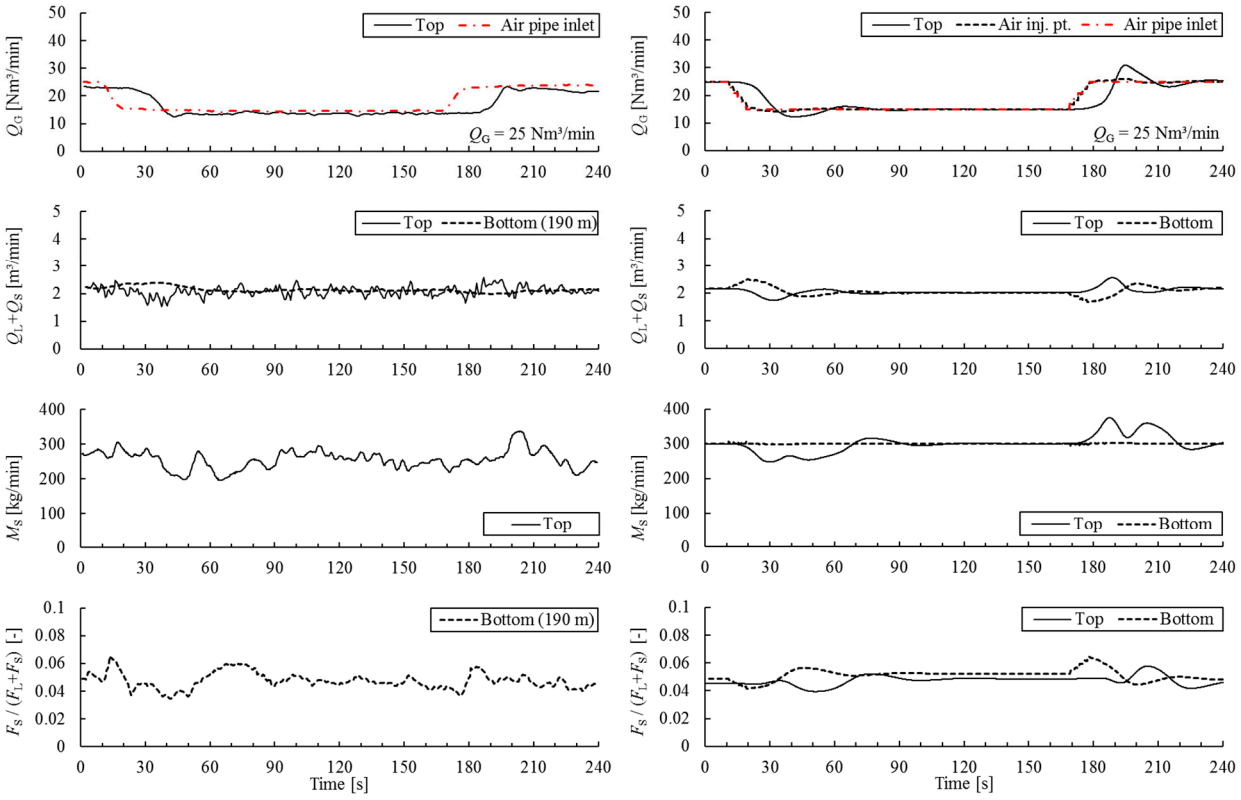

Figure 6. Unsteady flow characteristics of an air-lift pump when rapidly increasing and decreasing the air flow rate; the experimental result from the previous studies [12] (left panel) versus the calculated one (right panel).

Figure 7 shows the unsteady flow characteristics of an air-lift pump; the transient response of air flow rate (the first), slurry (water plus gravel) flow rate (the second), mass flow rate (the third), and volume fraction of gravel within the slurry (the fourth) when stopping the input of air for a while, while the system is at the steady state, i.e., 15 Nm³/min air flow rate, and 5% volume fraction of gravel. The graphs in the left panels show the experimental result from the previous study [12], and the ones in the right panel show the calculated one. When the air flow suddenly stops for about 15 s, the slurry flow rate at the top of the lifting pipe fluctuates significantly, and that at the bottom decreases to about half that at the steady state. The system recovers to its original conditions after restarting the air flow. The calculated result shows similar time transients compared with the experimental one, although the air flow rate peaks at the top of the lifting pipe during the transition period, as seen at the start-up stage (Figure 4).

Figure 8 shows the unsteady flow characteristics of an air-lift pump; the transient response of air flow rate (the first), slurry (water plus gravel) flow rate (the second), mass flow rate (the third), and volume fraction of gravel within the slurry (the fourth) when rapidly increasing and decreasing feed rate of gravel while the system is at the steady state, i.e., 15 Nm³/min air flow rate, and 5% volume fraction of gravel. The graphs in the left panel show the experimental result from the previous studies [13], and the ones in the right panel show the calculated one. The slurry flow rate decreases slightly at the bottom of the lifting pipe when the feed rate of gravel increases. The system reaches a steady state after all the gravel temporarily fed in the lifting pipe has been discharged. It takes 30 s for the gravel to go through from the inlet to the outlet of the lifting pipe. This trend is reversed when the feed rate of gravel decreases. Similar time transients are observed in the calculation.

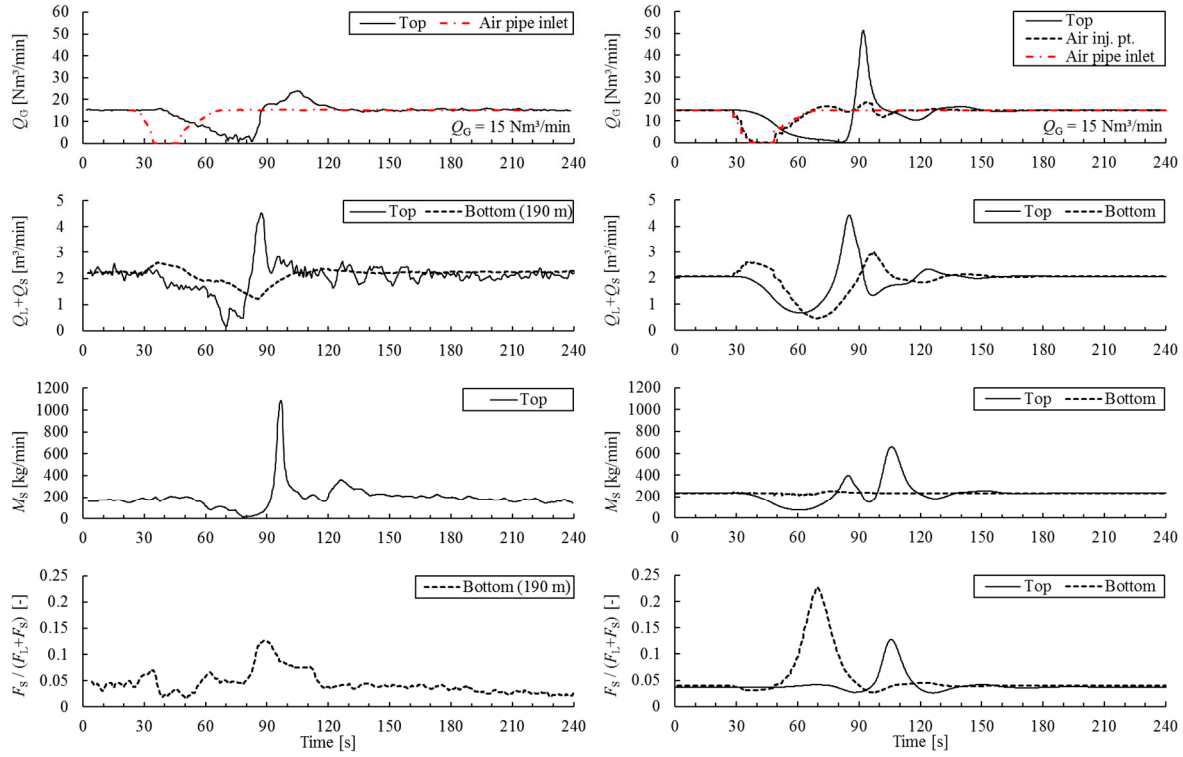

Figure 7. Unsteady flow characteristics of an air-lift pump when temporarily stopping input of air; the experimental result from the previous study [12] (left panel) versus the calculated one (right panel). Note that the solid, dashed, and dashed–dotted lines in each graph represent the same items shown in Figure 6.

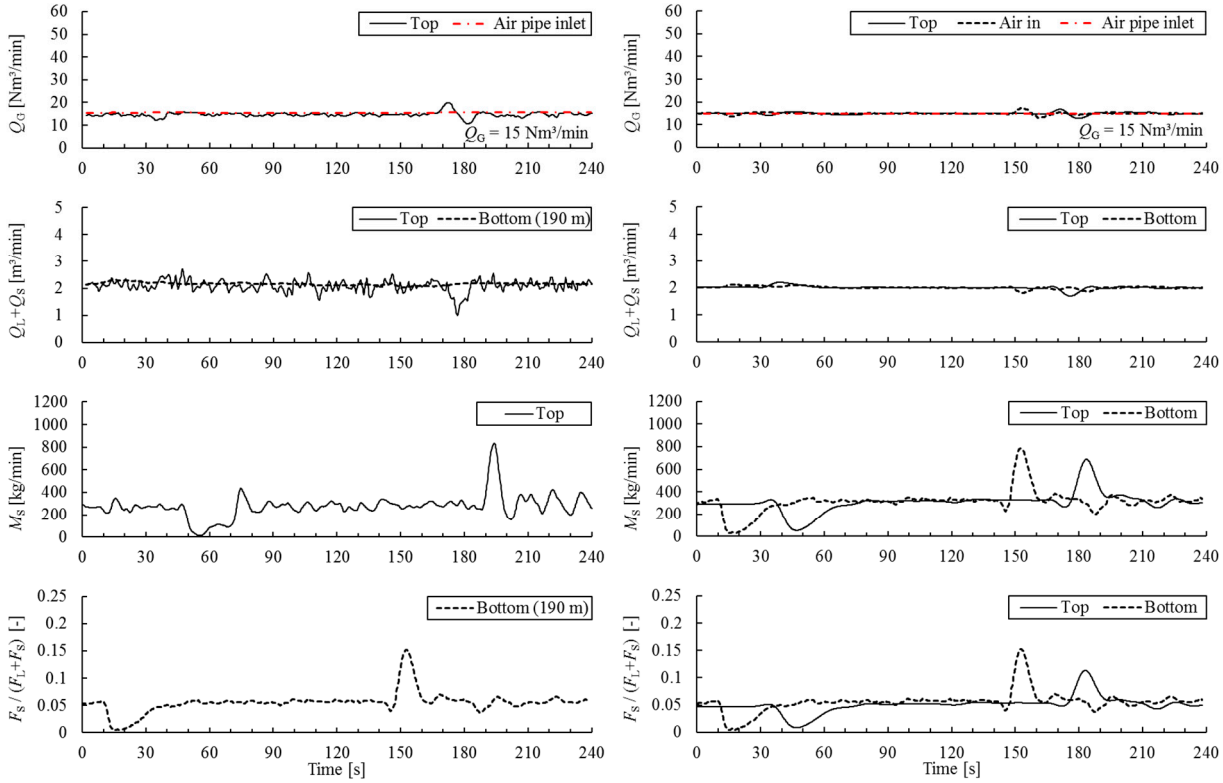

Figure 8. Unsteady flow characteristics of an air-lift pump when rapidly increasing and decreasing the feed rate of gravel; the experimental result from the previous studies [13] (left panel) vs. the calculated one (right panel). Note that the solid, dashed, and dashed–dotted lines in each graph represent the same items shown in Figure 6.

Figure 9 shows the unsteady flow characteristics of an air-lift pump; the transient response of air flow rate (the first), slurry (water plus gravel) (the second), mass flow rate (the third), and volume fraction of gravel within the slurry (the fourth) when changing feed rate of gravel periodically while the system is at the steady state, i.e., 15 Nm³/min air flow rate, and 5% volume fraction of gravel. The graphs in the left panel show the experimental results from the previous studies [13], and the ones in the right panel show calculated ones. When the feed rate of gravel changes periodically, the concentration of gravel in the lifting pipe fluctuates, and the fluctuation propagates to the outlet. However, there is little change in the slurry flow rate. This is because the period of the fluctuation—about 20 s—is shorter than the time required for gravel to move through the lifting pipe about 30 s. Moreover, the flow rate of discharged air fluctuates even though the air flow rate at the inlet of the air pipe is constant. This fluctuation is thought to occur at the air injection point too, and the irregularity of the lifting gravels causes it. The calculated result, the first graph in the right panel, shows the fluctuation of the air flow rate at the air injection points under a constant air flow rate at the inlet of the air pipe, which could not be found from the experimental result.

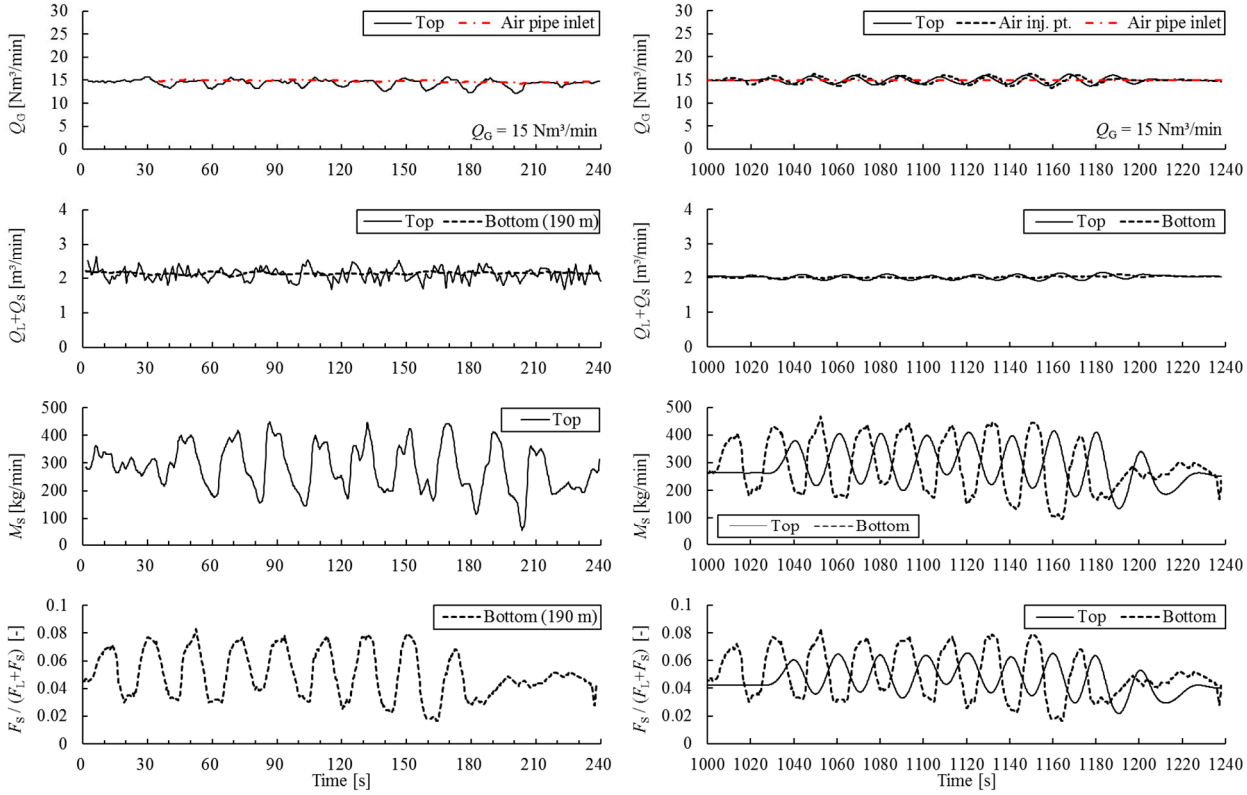

Figure 9. Unsteady flow characteristics of an air-lift pump when periodically changing the feed rate of gravel at the bottom; the experimental result from the previous studies [13] (left panel) versus the calculated one (right panel). Note that the solid, dashed, and dashed–dotted lines in each graph represent the same items shown in Figure 6.

4. Simulation on Hybrid Lifting Operation of Polymetallic Nodules and Rare-Earth Element-Rich Mud

4.1. Numerical Model

Figure 10 shows the dimensions of the numerical model and boundary conditions specified in the simulation. The diameter of the lifting pipe is larger than that of the previous study [4] to relate the simulation with a commercial production system operated in the 5500–5700 m deep sea around Minamitorishima island, and the conditions fit the

expected production rates of polymetallic nodules and REE-rich mud. The lifting pipe and the air pipe are placed vertically. The dimensions of the pipes are shown in Table 6. A total of 282 and 100 elements are created, respectively, by dividing the lifting pipe and the air pipe into equal lengths of 20 m. The mass flow rate of air is 36 kg/s. A velocity corresponding to the mass flow rate of air is specified at the inlet of the air pipe. The pressure at the air injection point by the lifting pipe analysis is specified at the outlet of the air pipe as a pressure boundary. The air is input into the lifting pipe through the air pipe at 2000 m water depth. A 0.5 MPa(G) pressure, which corresponds to the back pressure, is specified at the top. The hydrostatic pressure at 5600 m water depth is specified at the bottom. The physical properties of air, seawater, and those of REE-rich mud and polymetallic nodules are shown in Tables 7 and 8, respectively. Empirical equations for original REE-rich mud water [4], shown in Table 3, are used to evaluate the flow consistency index K and the flow behavior index n in the pseudo-plastic fluid. The method of Sato et al. [33,34] is used to calculate the drag coefficient for crushed polymetallic nodules.

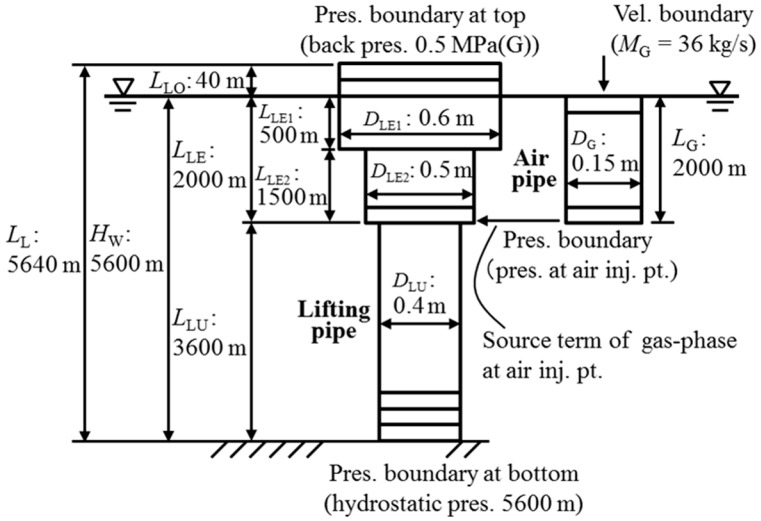

Figure 10. A numerical model and boundary conditions for simulation, lifting pipe (left), and air pipe (right).

Table 6. Pipe dimensions of the numerical model for simulation.

Lifting Pipe								Air Pipe	
H_W	L_L	L_{LO}	L_{LE}	L_{LU}	D_{LE1} H_W: 0–500	D_{LE2} 500–2000	D_{LU} 2000–5600	L_G	D_G
[m]	[m]	[m]	[m]	[m]	[m]	[m]	[m]	[m]	[m]
5600	5640	40	2000	3600	0.6	0.5	0.4	2000	0.15

Table 7. Physical properties, air, and seawater for simulation.

Material	Density	Viscosity	Surface Tension	Molecular Mass
	[kg/m³]	[Pa·s]	[N/m]	[kg/mol]
Air	Equation (10)	1.76×10^{-5}	7.4×10^{-2}	2.88×10^{-2}
Seawater	1.02×10^{3}	1.3×10^{-3}	-	-

Table 8. Physical properties, REE-rich mud, and polymetallic nodules for simulation.

Material	Density	Flow Consistency Index K	Flow Behavior index n	Particle Dia. D_P	Drag Coef. C_D
	[g/cm³]	[Pa.sⁿ]	[-]	[mm]	[-]

REE-Rich Mud	2.8	Eq. for Original REE-Rich Mud Water in Table 3	Eq. for Original REE-Rich Mud Water in Table 3	-	-
Polymetallic Nodules	2.0	-	-	20	1.17

The simulation proceeds following the actual operations. At the start-up stage, 36 kg/s mass flow rate of air is specified at the inlet of the air pipe. The air flow rate is increased linearly to 36 kg/s over 360 s to protect against irregular transient phenomena by sudden air flow change. The air flow rate at the outlet of the air pipe, calculated in the air pipe analysis, is used in the lifting pipe analysis by adding it as a source term of gas-phase in the lifting pipe element at the air injection point. The analysis continues until reaching a steady state. Next, 0.5 MPa(G) pressure is specified at the top of the lifting pipe as back pressure. The pressure is increased linearly to 0.5 MPa(G) over 360 s, and the analysis continues until reaching a steady state. REE-rich mud is then fed into the lifting pipe at a steady state under 36 kg/s mass flow rate of air and 0.5 MPa(G) back pressure. A constant volume concentration of REE-rich mud is specified at the bottom. The feed rate is increased linearly up to a specified feed rate over 360 s. Next, polymetallic nodules are fed into the lifting pipe specifying a volume fraction of the solid-phase at the bottom. This process is continued by increasing the feed rate gradually until reaching the maximum flow rate of polymetallic nodules. The time-step of the analysis is 4 s, and unsteady flow data, i.e., time transient data are recorded every 20 s.

4.2. Results and Discussion: Steady Flow Characteristics

Figure 11 shows the steady flow characteristics when lifting polymetallic nodules and REE-rich mud and hybrid lifting: slurry (seawater or REE-rich mud water plus polymetallic nodules) flux versus mass flow rate of polymetallic nodules and REE-rich mud. The solid lines show the cases of lifting polymetallic nodules (Case 1, colored in black) and REE-rich mud (Case 4, colored in red). The dashed line and the dashed–dotted line show the cases of hybrid lifting while the volume concentration of REE-rich mud C_X is kept at 2 (Case 2) and 3% (Case 3), respectively. While the mass feed rate of polymetallic nodules and REE-rich mud increases, the slurry flux gradually decreases. The mass flow rate of polymetallic nodules (Case 1) is larger than that of REE-rich mud (Case 4) at the same slurry flux. In hybrid lifting (Cases 2 and 3), when the mass flow rate of polymetallic nodules increases, that of REE-rich mud decreases as shown by the arrows in the graph, because slurry flux decreases.

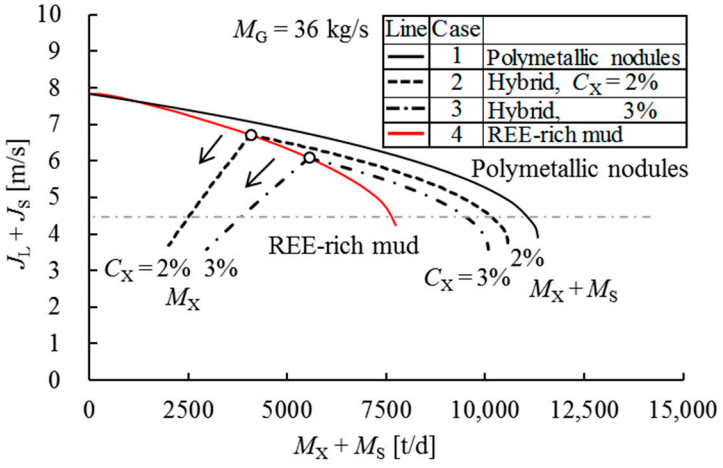

Figure 11. Steady flow characteristics of an air-lift pump for lifting polymetallic nodules and REE-rich mud, and both; hybrid lifting with 36 kg/s mass flow rate of air, and 0.5 MPa(G) back pressure.

Empirical equations for original REE-rich mud water [4], and a D_P of 20 mm and C_D of 1.17 for polymetallic nodules are used.

Table 9 summarizes the results and comparison of lifting performance at 36 kg/s mass flow rate of air, 0.5 MPa(G) back pressure, and 4.5 m/s slurry flux. The power requirements N_{Power} and efficiency η are defined by Equations (11) and (12), respectively. The total mass flow rate and the efficiency are 11,020 t/d, 0.378 for Case 1; 10,140 t/d (7620 t/d: polymetallic nodules, 2520 t/d: REE-rich mud), 0.373 for Case 2; 9480 t/d (5610 t/d: polymetallic nodules, 3870 t/d: REE-rich mud), 0.364 for Case 3; and 7600 t/d, 0.338 for Case 4. The total mass flow rate and the efficiency increase when the ratio of the mass flow rate of polymetallic nodules increases under the same slurry flux, which is the same tendency as that shown by a simulation of a smaller-scaled system [4]. The power requirement is about 9.3 MW and the mixture velocity at the exit of the lifting pipe is 19.2 m/s for all the cases.

$$N_{Power} = \frac{R}{M}(T + 273.15)\ln\frac{P_{Gout}}{P_{Gin}}M_G \quad (11)$$

$$\eta = \frac{(\rho_X C_X Q_L + \rho_S Q_S) g L_{LO} + ((\rho_X - \rho_{L0}) C_X Q_L + (\rho_S - \rho_{L0}) Q_S) g (L_{LE} + L_{LU})}{N_{Power}} \quad (12)$$

where P_{Gout}: pressure at the outlet of the air pipe [Pa]; P_{Gin}: pressure at the inlet of the air pipe [Pa].

Table 9. Summary of lifting performances at 36 kg/s mass flow rate of air, 0.5 MPa(G) back pressure, and 4.5 m/s slurry plus solid flux.

Case	$M_X + M_S$	M_X	M_S	C_X	C_S	$J_{M\ exit}$	N_{power}	η
	[kt/d]	[kt/d]	[kt/d]	[%]	[%]	[m/s]	[MW]	[-]
1	11.02	0	11.02	0	11.33	19.2	9.26	0.378
2	10.14	2.52	7.62	2.00	7.79	19.2	9.26	0.373
3	9.48	3.87	5.61	3.00	5.74	19.2	9.26	0.364
4	7.60	7.60	0	5.59	0	19.2	9.27	0.338

M_X: mass flow rate of REE-rich mud; M_S: mass flow rate of polymetallic nodules; C_X: volume concentration of REE-rich mud; C_S: volume concentration of polymetallic nodules; J_{Mexit}: mixture flux at exit; N_{Power}: power requirements; η: efficiency.

4.3. Results and Discussion: Unsteady Flow Characteristics at Operation

Figure 12 shows the unsteady flow characteristics of an air-lift pump; the transient response of air flow rate (the first), seawater flow rate (the second), and pressure (the third, only right panel) when beginning the input of air from the air pipe inlet at 36 kg/s mass flow rate of air (left panel) and when setting 0.5 MPa(G) back pressure after that (right panel). In the first graph of both panels, the solid line: air flow rate at the top of the lifting pipe, the dashed line: at the air injection point, and the dashed–dotted line: at the inlet of the air pipe, i.e., specified air flow rate. In the second graph of both panels, the solid line: seawater flow rate at the top of the lifting pipe, and the dashed line: at the bottom. In the third graph (only right panel), the solid line: back pressure specified at the top. Seawater begins to discharge at the top 180 s after the beginning of the input of air. The maximum flow rates of air and seawater are 3.66 and 3.38 times larger, respectively, than those at the steady state. The system reaches a steady state after 1500 s. When the back pressure increases from 0 to 0.5 MPa(G) over 360 s, the seawater flow rate gradually decreases and then reaches a steady state. Air flow at the top fluctuates slightly.

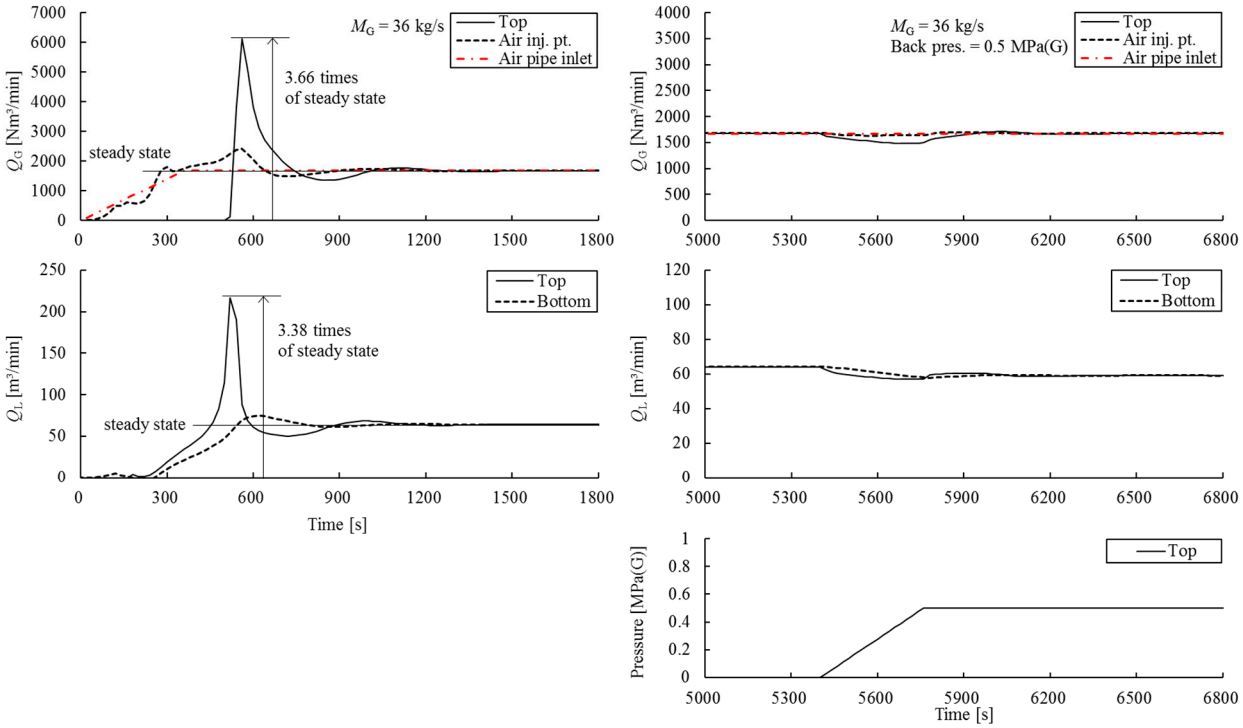

Figure 12. Unsteady flow characteristics of an air-lift pump at start-up, i.e., when beginning the input of air at 36 kg/s mass flow rate of air (left panel), followed by specifying 0.5 MPa(G) back pressure (right panel).

Figure 13 shows the unsteady flow characteristics of an air-lift pump; the transient response of air flow rate (the first), slurry flow rate (the second), mass flow rate of REE-rich mud (the third), and polymetallic nodules (the fourth, only right panel) when beginning the feed of REE-rich mud at 2% volume concentration (left panel) and when beginning the feed of polymetallic nodules at 87.7 kg/s while keeping 2% volume concentration of REE-rich mud (right panel). The mass flow rate of air is 36 kg/s, and the back pressure is 0.5 MPa(G). In the first graph of both panels, the solid line: air flow rate at the top of the lifting pipe, the dashed line: at the air injection point, and the dashed–dotted line: at the inlet of the air pipe, i.e., specified air flow rate. In the second graph, the solid line: slurry (seawater or mud water plus polymetallic nodules) flow rate at the top, and the dashed line: at the bottom. In the third graph, the solid line: mass flow rate of REE-rich mud at the top, the dashed line: at the bottom, and the dashed–dotted line: volume concentration of REE-rich mud at the bottom. In the fourth graph (only right panel), the solid line: mass flow rate of polymetallic nodules at the top, and the dashed line: at the bottom. In both cases, the slurry flow rate gradually decreases after they begin to be fed at the bottom. It takes 720 s and 760 s, respectively, to lift REE-rich mud and polymetallic nodules from the bottom to the top. The mass flow rates of both REE-rich mud and polymetallic nodules at the top gradually increase. The rate of increase at the top is slower than that specified at the bottom because REE-rich mud and polymetallic nodules are dispersed during lifting. It takes 1320 s and 3680 s to reach the steady state after beginning the feed, respectively. When beginning the feed of polymetallic nodules while keeping a 2% volume concentration of REE-rich mud, the mass flow rate of REE-rich mud gradually decreases (right panel).

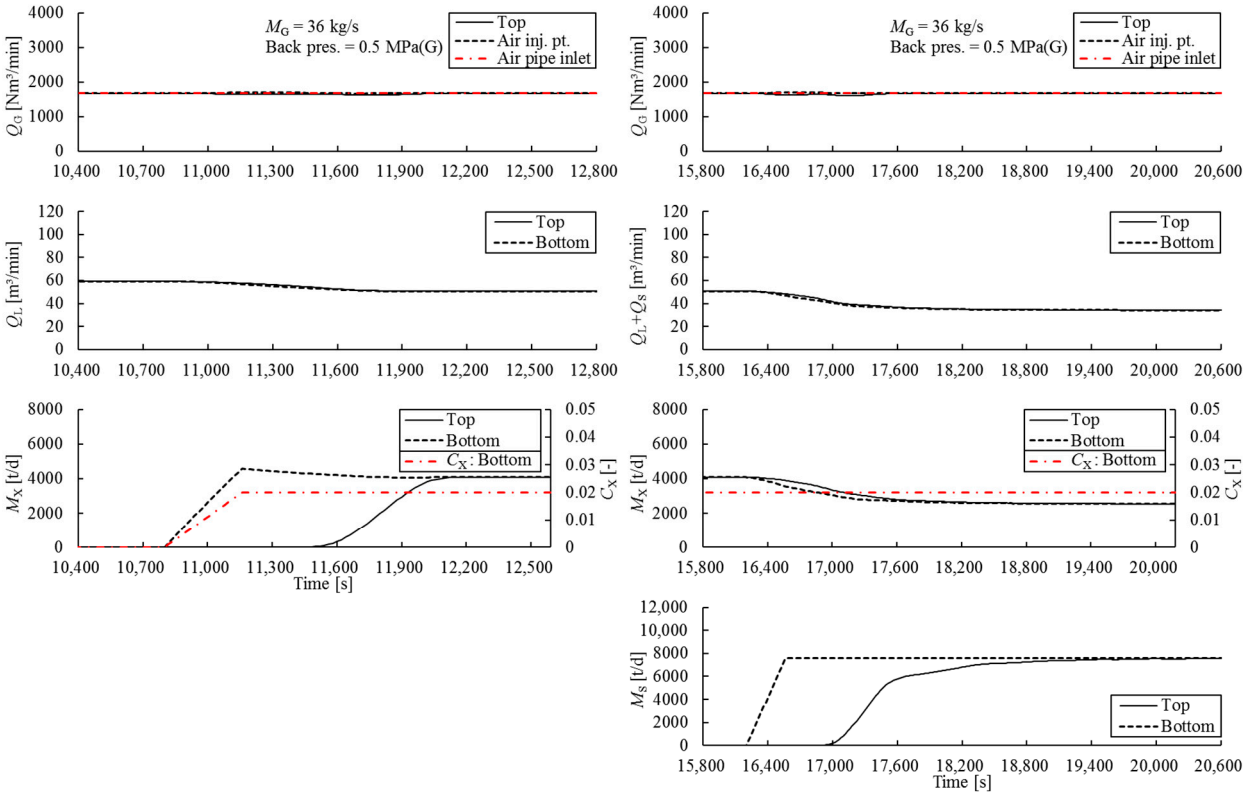

Figure 13. Unsteady flow characteristics of an air-lift pump when beginning the feed of REE-rich mud (left panel) and polymetallic nodules (right panel) with 36 kg/s mass flow rate of air and 0.5 MPa(G) back pressure.

Figure 14 shows the unsteady flow characteristics of an air-lift pump; the transient response of air flow rate (the first), slurry flow rate (the second), mass flow rate of REE-rich mud (the third), and polymetallic nodules (the fourth, only left panel) when stopping the feed of polymetallic nodules while keeping a 2% volume concentration of REE-rich mud (left panel), and when stopping the feed of REE-rich mud (right panel). The mass flow rate of air is 36 kg/s, and the back pressure is 0.5 MPa(G). In both cases, the mass flow rates at the top of the lifting pipe temporally increase by a factor of 1.38 for polymetallic nodules and 1.11 for REE-rich mud over those at the steady state, and then decreases to zero finally over 1000 s (polymetallic nodules, left panel) and 900 s (REE-rich mud, right panel). The slurry flow rate gradually increases while the mass feed flow rates decrease.

Figure 15 shows the unsteady flow characteristics of an air-lift pump; the transient response of air flow rate (the first), seawater flow rate (the second), and pressure (the third, only left panel) when releasing 0.5 MPa(G) back pressure (left panel) and when stopping the input of air at the air pipe inlet from 36 kg/s mass flow rate of air (right panel) over 360 s. When releasing the back pressure, the seawater flow rate gradually increases and reaches a steady state. When stopping the input of air, the seawater flow rate gradually decreases, even though seawater continues to discharge for a while before finally reaching zero after 720 s.

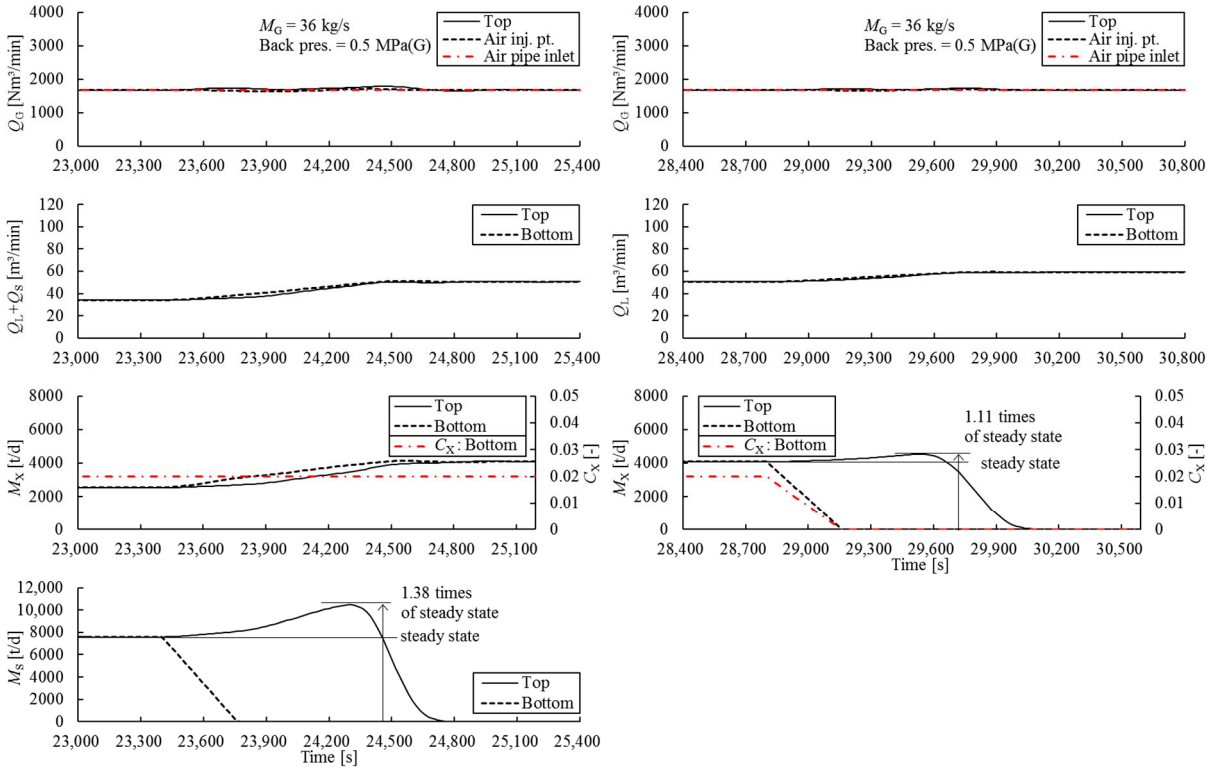

Figure 14. Unsteady flow characteristics of an air-lift pump when stopping the feed of polymetallic nodules (left panel) and REE-rich mud (right panel), with 36 kg/s mass flow rate of air, 0.5 MPa(G) back pressure, 2% volume concentration of REE-rich mud, and 87.7 kg/s feed rate of polymetallic nodules. Note that the solid, dashed, and dashed–dotted lines in each graph represent the same items shown in Figure 13.

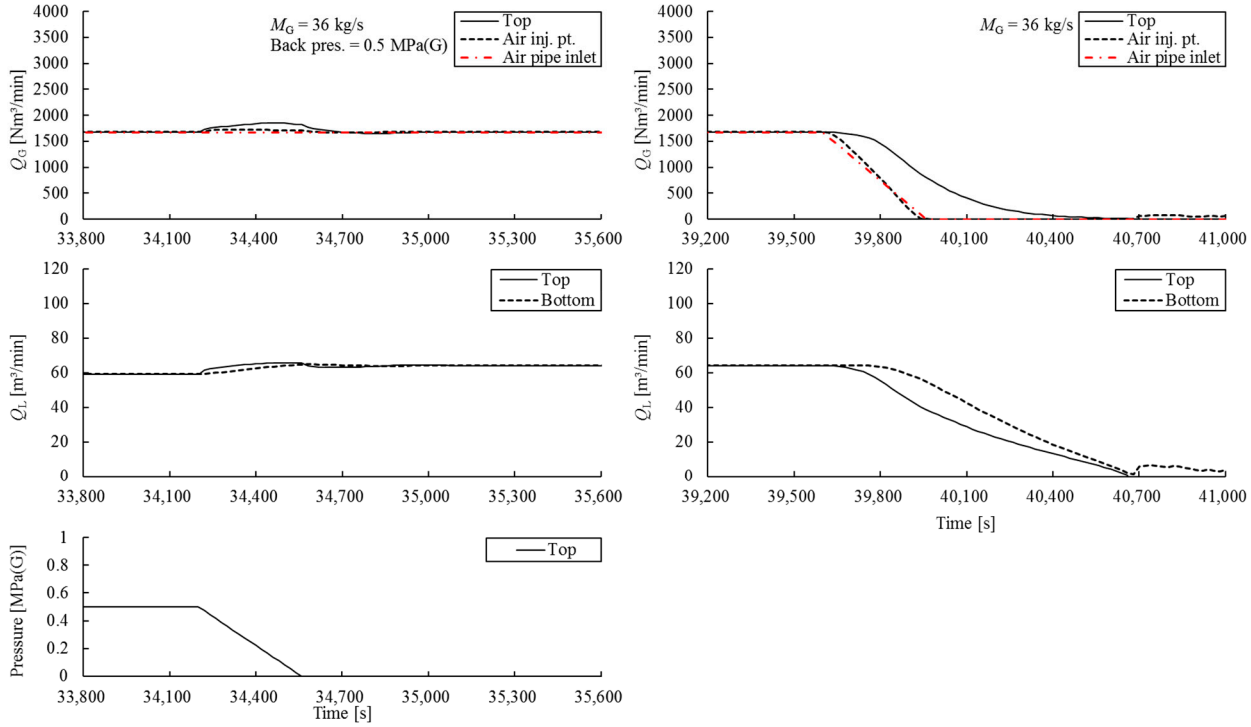

Figure 15. Unsteady flow characteristics of an air-lift pump at shut-down, i.e., releasing back pressure from 0.5 MPa(G) to zero (left panel) and stopping the input of air from 36 kg/s (right panel). Note that the solid, dashed, and dashed–dotted lines in each graph represent the same items shown in Figure 12.

4.4. Results and Discussion: Unsteady Flow Characteristics Associated with Disturbances

Figure 16 shows the unsteady flow characteristics of an air-lift pump; the transient response of air flow rate (the first), slurry flow rate (the second), mass flow rate of REE-rich mud (the third), and polymetallic nodules (the fourth) when changing the feed rate of polymetallic nodules periodically. The disturbance follows a sinusoidal wave, with amplitude from the steady state of 25.0 kg/s, and a period of 300–1200 s at 36 kg/s air flow rate, 0.5 MPa(G) back pressure, 2% volume concentration of REE-rich mud, and 87.7 kg/s feed rate of polymetallic nodules. The graphs in the left panel show the result for a disturbance with a 300 s period, and the ones in the right panel show the results for an 800 s period. Figure 17 shows the normalized magnitude of the fluctuations in the mass flow rate of polymetallic nodules (the first) and the mixture, i.e., air plus slurry flow rate (the second). The time series data for fifty periods were analyzed at 4 s intervals by the discrete Fourier Transform (DFT) function embedded in NumPy ver.1.21.2 under Python ver.3.9.7 [34]. When the feed rate of polymetallic nodules changes periodically, the concentration of polymetallic nodules in the lifting pipe fluctuates, and the fluctuation propagates to the top. If the fluctuation period is longer than the time required for passage through the lifting pipe, 760 s for polymetallic nodules as shown in Figure 13, the fluctuation in the concentration of polymetallic nodules propagates to the same amount. If the period is shorter, then the fluctuation in concentration is averaged during transport through the lifting pipe and attenuated at the top. Also, the flow of each phase fluctuates along the lifting pipe. In particular, at a period of 700 to 900 s, which is close to the transit time through the lifting pipe, the magnitude is larger than that in the rest of the range of periods (the second graph in Figure 17). On the other hand, the magnitude is small at periods shorter than the time required for passage through the lifting pipe, which is consistent with the experimental results as shown in Figure 9. The fact that the air flow fluctuates at the air injection point, even though the air flow rate at the air pipe inlet is constant, is also one of the reasons that the fluctuations grow in the lifting pipe.

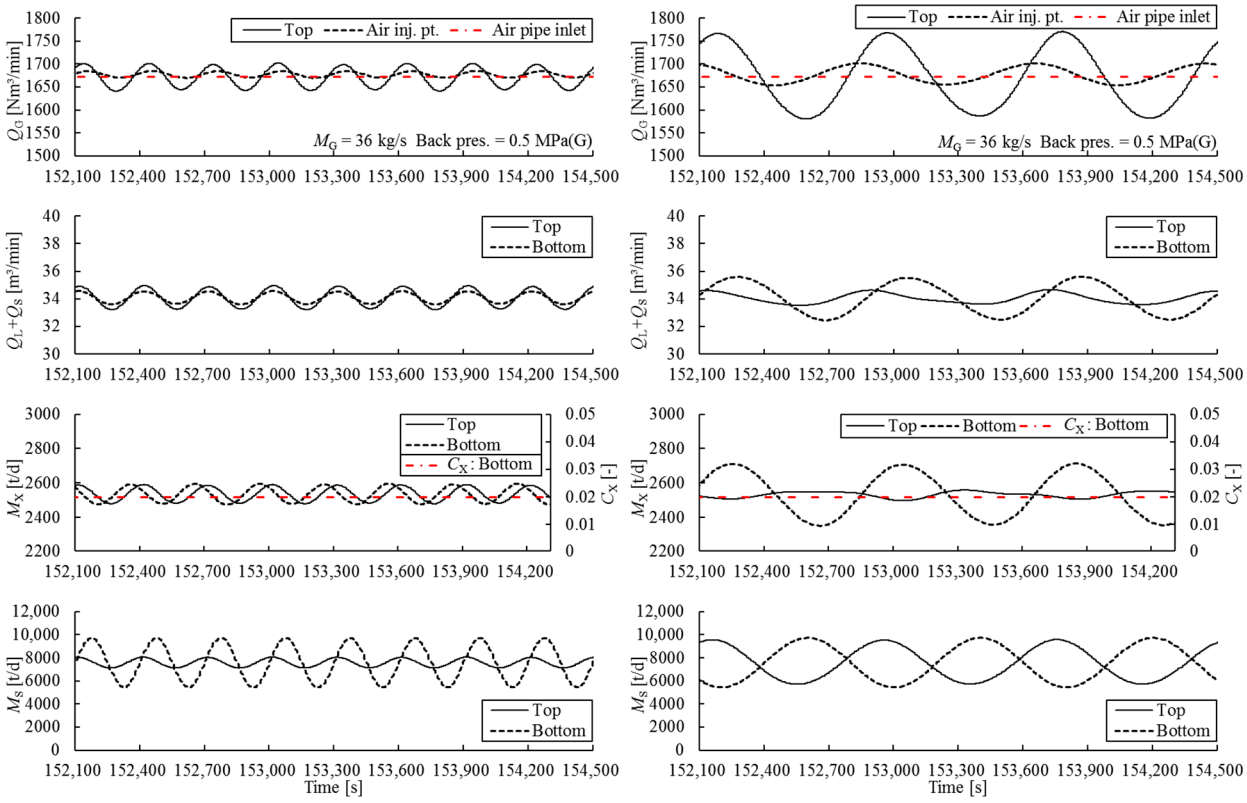

Figure 16. Unsteady flow characteristics of an air-lift pump; the transient response against a disturbance; periodic fluctuations of the feed rate of polymetallic nodules following a sinusoidal wave with a period of 300 s (left panel) and 800 s (right panel) at 36 kg/s mass flow rate of air, 0.5 MPa(G) back pressure, 2% volume concentration of REE-rich mud, and 87.7 kg/s feed rate of polymetallic nodules. Note that the solid, dashed, and dashed–dotted lines in each graph represent the same items shown in Figure 13.

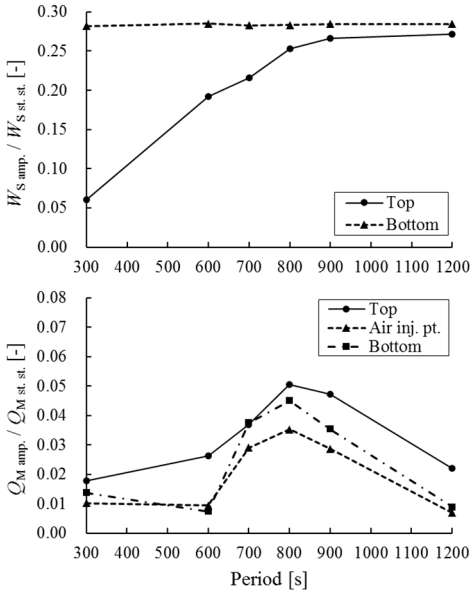

Figure 17. Normalized amplitudes of mass flow rate of polymetallic nodules (the first), and mixture (air plus slurry) flow rate (the second) for each period of disturbance. Note that subscript "st. st." means steady state.

5. Conclusions

The unsteady flow characteristics and the performances of a production system with an air-lift pump for lifting polymetallic nodules and REE-rich mud under the 5500–5700 m seabed around Minamitorishima island were investigated by numerical analyses. The one-dimensional drift–flux model was used to solve the gas–liquid–solid three-phase flow and gas–liquid flow in the lifting pipe.

First, the reliability of the schemes and the program was verified by comparing the numerical results of unsteady flow characteristics, i.e., the transient response of the air-lift pump with the experimental ones. The numerical results represented the unsteady flow characteristics of the experimental ones well.

Next, numerical simulations were conducted. The simulation model is related to a commercial production system operated in the deep sea around Minamitorishima island, and the conditions used in the simulations fit the expected production rates. The following lifting performances for the commercial production system were derived under the dimensions of the air-lift pump:

Length of the lifting pipe: 5640 m;
Water depth of the lifting pipe: 5600 m;
Water depth at the air injection point: 2000 m;
Diameter is below the air injection point: 0.4 m;
Diameter above the air injection point: 0.5 m;
Diameter above a 500 m water depth: 0.6 m.
and operational conditions:
Mass flow rate of air: 36 kg/s;

Back pressure: 0.5 MPa(G);
Slurry (seawater or REE-rich mud water plus polymetallic nodules) flux: 4.5 m/s;
Polymetallic nodules: D_P of 20 mm, C_D of 1.17;
REE-rich mud: original mud water without pre-processing.

In the case of lifting polymetallic nodules, the production rate (total mass flow rate) is 11,020 t/d, the volume concentration of polymetallic nodules is 11.33%, and the efficiency is 0.378.

In the case of hybrid lifting, while keeping a 2% volume concentration of REE-rich mud, the production rate is 10,140 t/d (polymetallic nodules: 7620 t/d, REE-rich mud: 2520 t/d), the volume concentration of nodules is 7.79%, and the efficiency is 0.373.

In the case of hybrid lifting, while keeping a 3% volume concentration of REE-rich mud, the production rate is 9480 t/d (polymetallic nodules: 5610 t/d, REE-rich mud: 3870 t/d), the volume concentration of nodules is 5.74%, and the efficiency: 0.364.

In the case of lifting REE-rich mud, the production rate is 7600 t/d, the volume concentration of REE-rich mud is 5.59%, and the efficiency is 0.338.

The power requirement is about 9.3 MW and the mixture velocity at the exit of the lifting pipe is 19.2 m/s for all the cases.

The unsteady characteristics of the air-lift pump for the commercial production system, such as at start-up, shut-down, and when starting or stopping the feed of polymetallic nodules and REE-rich mud were evaluated. The following were concluded from the simulations regarding the unsteady flow characteristics of the system:

(1) Regarding the start-up and shut-down stages, seawater begins to discharge at the top of the lifting pipe 180 s after beginning the input of air from the air pipe inlet at 36 kg/s mass flow rate of air. The maximum flow rates of air and seawater are higher by factors 3.66 and 3.38, respectively, than those at a steady state. The system reaches a steady state after 1500 s. When the air input at the air pipe inlet is stopped from the 36 kg/s mass flow rate of air, the seawater flow rate gradually decreases, even though seawater continues to discharge for a while, finally reaching zero after 720 s.

(2) Regarding the feed of polymetallic nodules and REE-rich mud starting and stopping, the slurry flow rate gradually decreases when beginning the feed of REE-rich mud at 2% volume concentration, and when beginning the feed of polymetallic nodules at 87.7 kg/s while keeping a 2% volume concentration of REE-rich mud. It takes 720 s and 760 s, respectively, to lift REE-rich mud and polymetallic nodules from the bottom to the top of the lifting pipe. The mass flow rate of both REE-rich mud and polymetallic nodules at the top gradually increases. The rate of increase at the top is slower than that specified at the bottom because REE-rich mud and polymetallic nodules are dispersed during lifting. When the feed of polymetallic nodules stops while keeping a 2% volume concentration of REE-rich mud, and when the feed of REE-rich mud stops, the mass flow rates at the top of the lifting pipe temporally increase by a factor 1.38 (polymetallic nodules) and 1.11 (REE-rich mud) over those at steady state and then decreases to zero finally over 1000 s (polymetallic nodules) and 900 s (REE-rich mud). The slurry flow rate gradually increases while the mass feed flow rates decrease.

(3) Regarding associated disturbances, when the feed rate of polymetallic nodules changes periodically, the concentration of polymetallic nodules in the lifting pipe fluctuates, and the fluctuation propagates to the top. If the fluctuation period is longer than the time required for passage through the lifting pipe: 760 s for polymetallic nodules, the fluctuation in the concentration of polymetallic nodules propagates to the same amount. If the period is shorter, then the fluctuation in

concentration is averaged during transport through the lifting pipe and attenuated at the top. Also, the flow of each phase fluctuates along the lifting pipe. In particular, at a period of 700 to 900 s, which is close to the transit time through the lifting pipe, the magnitude is larger than that in the rest of the range of periods. In contrast, the magnitude is small at periods shorter than the time required for passage through the lifting pipe, which is consistent with the experimental results. The air flow fluctuates at the air injection point, even though the air flow rate at the inlet of the air pipe is constant. This is also one of the reasons for the increase in the fluctuation in the lifting pipe.

In this study, we demonstrated that the program and the schemes could simulate the unsteady flow characteristics and the lifting performance of a commercial production system using an air-lift pump for the hybrid lifting well, and they could derive useful information and know-how in advance for safely and continuously operating the system. They would enable one to optimize the design and the operation of the hybrid lifting using an air-lift pump by considering not only increasing the efficiency technically and the benefits economically but also suppressing the environmental disturbance in the deep sea if further studies are advanced.

Author Contributions: Y.S.: conceptualization, methodology, software, validation, formal analysis, investigation resources, data curation, writing—original draft preparation, writing—review and editing, visualization, supervision, and project administration. M.S.: software, validation, formal analysis, investigation, resources, data curation, writing—original draft preparation, writing—review and editing, and visualization. K.F.: resources, writing—review and editing, funding acquisition. K.N.: writing—review and editing, and funding acquisition. Y.K.: writing—review and editing and funding acquisition. All the authors have read and agreed to the published version of the manuscript.

Funding: The organization of this study was funded by the Consortium for the Promotion of REE-rich Mud and Manganese Nodule Development at the University of Tokyo.

Institutional Review Board Statement: Not applicable.

Informed Consent Statement: Not applicable.

Data Availability Statement: Data are unavailable for privacy reasons.

Acknowledgments: This study was promoted by the Consortium for the Promotion of REE-rich Mud and Manganese Nodule Development at the University of Tokyo. We express our thanks to all the people involved in the work. We also sincerely thank Tadashi Masuyama and Nobuo Hatakeyama for their valuable discussions. We referenced the results of the research and development regarding the air-lift pumping system previously conducted under The Manganese Nodule Mining System, a Japanese national project. We sincerely respect the researchers and the engineers who worked on that project at the Technical Research Institute and the design offices of the Hitachi Zosen Corporation for their efforts.

Conflicts of Interest: The authors declare no conflicts of interest.

Nomenclature

C_{D}	drag coefficient of particle [-]
C_{k0}	parameter to calculate drift velocities of the k-phase $(k=\mathrm{G},\mathrm{S})$ [-]
C_{S}	volume concentration of polymetallic nodules [-]
C_{X}	volume concentration of (REE-rich) mud within liquid-phase $\left(\equiv F_{\mathrm{X}}/F_{\mathrm{L}}\right)$ [-]

D	a representative pipe diameter of lifting pipe [m]
D_{G}	pipe diameter of air pipe [mm, m]
D_{L}	pipe diameter of lifting pipe [mm]
D_{LE1}	pipe diameter at range of L_{LE1} [m]
D_{LE2}	pipe diameter at range of L_{LE2} [m]
D_{LU}	pipe diameter at range of L_{LU} [m]
D_{P}	particle diameter [mm]
F_k	volume fraction of the k -phase $(k = \mathrm{G}, \mathrm{L}, \mathrm{S})$ [-]
g	gravitational acceleration [m/s^2]
H_{W}	water depth of air-lift pump (length of lifting pipe from sea surface to bottom) [m]
J_k	flux of the k -phase $(k = \mathrm{G}, \mathrm{L}, \mathrm{S})$ [m/s]
J_{M}	mixture flux [m/s]
J_{Mexit}	mixture flux at exit [m/s]
K	flow consistency index $[\mathrm{Pa} \cdot \mathrm{s}^{\mathrm{n}}]$
L	a representative length in axial direction of lifting pipe [m]
L_{G}	total length of air pipe [m]
L_{L}	total length of lifting pipe [m]
L_{LE}	length of lifting pipe from sea surface to air injection point [m]
L_{LE1}	length of lifting pipe from sea surface to 500 m water depth [m]
L_{LE2}	length of lifting pipe from 500 m water depth to air injection point [m]
L_{LO}	length of lifting pipe above sea surface [m]
L_{LU}	length of lifting pipe under air injection point [m]
M	molecular weight, air: 2.88×10^{-2} [kg/mol]
M_{G}	mass flow rate of air [kg/s]
M_{S}	mass flow rate of polymetallic nodules [t/d]
M_{X}	mass flow rate of REE-rich mud [t/d]
N_{Power}	power requirements of air compressor [W]
n	flow behavior index [-]
$P_{\mathrm{at.}}$	atmospheric pressure, 1.01×10^5 [Pa]
P_{G}	pressure in air pipe [Pa]
P_{Gout}	pressure at outlet of air pipe [Pa]
P_{Gin}	pressure at inlet of air pipe [Pa]
P_{M}	pressure of mixture in lifting pipe [Pa]
Q_{G}	air flow rate [Nm^3/min]
R	gas constant, 8.3145 [J/(mol·K)]
T	temperature [degrees (Celsius)]
t	time [s]
V_k	velocities of the k -phase $(k = \mathrm{G}, \mathrm{L}, \mathrm{S})$ [m/s]
V_{kj}	parameter to calculate drift velocities of the k -phase $(k = \mathrm{G}, \mathrm{S})$ [m/s]
V_{k_dfj}	drift velocities of the k -phase $(k = \mathrm{G}, \mathrm{S})$ (velocities of the k -phase $(k = \mathrm{G}, \mathrm{S})$ relative to mixture flux) [m/s]
V_{M}	center-of-mass velocity of mixture [m/s]
V_{SS}	terminal velocity of particle [m/s]

W_k	velocities of the k-phase $(k = \mathrm{G, L, S})$ relative to the center-of-mass velocity of mixture $\left(\equiv V_k - V_\mathrm{M}\right)$ [m/s]
Z_a	parameter in Akagawa's formula [-]
z	coordinate in the axial direction of lifting pipe, from bottom to top [m]
Greek Letters	
Γ_k	source term of the k-phase $(k = \mathrm{G, L, S})$ per unit volume [kg/(m^3· s)]
$\dot{\gamma}$	shear rate [s^{-1}]
ΔP_L	pressure drop by flowing liquid-phase with liquid flux [Pa]
ΔP_M	pressure drop of mixture [Pa]
Δt	time-step [s]
ε	porosity $\left(\equiv F_\mathrm{L}/\left(F_\mathrm{L} + F_\mathrm{S}\right)\right)$ [-]
η	efficiency of air compressor [-]
λ	pipe friction factor [-]
μ_0	viscosity of seawater [Pa·s]
ρ_M	density of mixture [kg/m^3]
ρ_k	density of the k-phase$(k = \mathrm{G, L, S})$ [kg/m^3]
τ	shear stress [Pa]
τ_W	shear stress by pipe friction [Pa]
Subscripts	
G	gas-phase
L	liquid-phase
S	solid-phase
Abbreviations	
UF	underflow mud water, which contains high concentrations of REEs

References

1. Iijima, K.; Yasukawa, K.; Fujinaga, K.; Nakamura, K.; Machida, S.; Takaya, Y.; Ohta, J.; Haraguchi, S.; Nishio, Y.; Usui, Y.; et al. Discovery of extremely REY-rich mud in the western North Pacific Ocean. *Geochem. J.* **2016**, *50*, 557–573.
2. Machida, S.; Fujinaga, K.; Ishii, T.; Nakamura, K.; Hirano, N.; Kato, Y. Geology and geochemistry of ferromanganese nodules in the Japanese Exclusive Economic Zone around Minamitorishima Island. *Geochem. J.* **2016**, *50*, 539–555.
3. Yasukawa, K. Geochemical features of Fe-Mn micronodules in deep-sea sediments of the western North Pacific Ocean: Potential for co-product metal extraction from REY-rich mud. *Ore Geol. Rev.* **2020**, *127*, 103805.
4. Shimizu, Y.; Sugihara, M.; Fujinaga, K.; Nakamura, K.; Kato, Y. Air-Lift Pumping System for Hybrid Mining of Rare-Earth Elements-Rich Mud and Polymetallic Nodules around Minamitorishima Island. *J. Mar. Sci. Eng.* **2024**, *12*, 1470.
5. Weber, M.; Dedegil, Y. Transport of Solids according to the Air-lift Principle. In Proceedings of the 4th International Conference on the Hydraulic Transport of Solids in Pipes, Alberta, Canada, 18–21 May 1976; pp. H1-1–H1-23.
6. Allseas. Trial Run Concludes with Record Haul. 2022. Available online: https://allseas.com/news/trial-run-concludes-withrecord-haul/ (accessed on 19 November 2024).
7. Allseas. Successful Conclusion of Pilot Polymetallic Nodules Collection System Trials on Allseas' Hidden Gem. 2022. Available online: https://www.youtube.com/watch?v=yPXiEFejJnk (accessed on 19 November 2024).
8. Yamaji, N.; Okamoto, N.; Shiokawa, S.; Kawano, S.; Sakurai, H. Achievement for Pilot Test of Excavating and Ore Lifting Conducted for Seafloor Polymetallic Sulphides–World's First Success in Continuous Ore Lifting Test for Seafloor Polymetallic Sulphides. *J. MMIJ* **2019**, *135*, 42–51.
9. Yamazaki, T.; Tsurusaki, K.; Handa, K.; Tomishima, Y. Fundamental Study of Design Parameters for Manganese Nodule Collector. *Shigen Kankyou* **1999**, *8*, 19–24.
10. Saito, T.; Kajishima, T. Studies on Lifting of Manganese Nodules by Air-Lift Pump. *Shigen Kankyou* **1999**, *8*, 5–17.

11. Ikegami, K.; Wada, Y.; Yasukawa, H.; Minami, T. Research and Development of Total System for Manganese-Nodule Mining System. *Shigen Kankyou* **1999**, *8*, 99–108.
12. Yokogawa, A.; Suzuki, M.; Tojo, C.; Shimizu, Y. A Study on Unsteady Characteristics of Air-Lift Mining System [Earifuto Youkousouchi no Hiteijou Tokusei ni Kansuru Kenkyu]. In Proceedings of the MMIJ Fall Meeting, Japan, 1985; Volume E-4, pp. 9–12.
13. Shimizu, Y.; Ishimaru, H.; Shimizu, T.; Tojo, C.; Suzuki, M.; Yokogawa, A.; Saito, T. Control of Air-Lift Pumping System Used for Manganese Nodule Mining. In Proceedings of the 3rd International Conference on Multi-Phase Flow, Lyon, France, 8–12 June 1998.
14. Miyazaki, E.; Kawamura, Y.; Sawada, I.; Kyo, M.; Akiyama, K. The result of the seabed mud lifting performance test by the SIP rare-earth mud mining system. In Proceedings of the MMIJ Fall Meeting 2023, Matsuyama, Japan, 12–14 September 2023.
15. The University of Tokyo. *The Consortium for Promotion of REE-Rich Mud and Manganese Nodule Development*; Annual Report FY2023; The University of Tokyo: Tokyo, Japan, 2024.
16. Shimizu, K.; Takagi, S. Study on the Performance of a 200m Airlift Pump for Water and Highly-viscous Shear-thinning Slurry. *Int. J. Multiph. Flow* **2012**, *142*, 103726.
17. Hatakeyama, N. Numerical Analysis on Air-Lift Pumping System for Mining Rare-Earth Rich Mud. Ph.D. Thesis, Tohoku University, Sendai, Japan, 1995.
18. Hatakeyama, N.; Takahashi, H.; Saito, T.; Masuyama, T. A Numerical Simulation of Unsteady Flow in an Air-lift Pump for Lifting Deep-sea Mineral Resources. *J. MMIJ* **1999**, *115*, 958–964.
19. Hibiki, T.; Ishii, M. One-Dimensional Drift-Flux Model and Constitutive Equations for Relative Motion between Phases in Various Two-Phase Flow Regimes. *Int. J. Heat Mass Transf.* **2003**, *46*, 4935–4948.
20. Thermal Hydraulics Division; AESJ. *Numerical Analysis of Gas-Liquid Two-Phase Flow [Kieki Nisouryu no Suuchi Kaiseki]*; Asakura Shoten: Tokyo, Japan, 1993; pp. 35–53.
21. Ito, S. *Fluid Engineering*; Maruzen: Tokyo, Japan, 1970; pp. 88–90.
22. Wen, C.Y.; Yu, Y.H. Mechanics of Fluidization. *Chem. Eng. Prog. Symp. Ser.* **1966**, *62*, 100–111.
23. Akagawa, K. *Gas-Liquid Two-Phase Flow [Kieki Nisouryu]*; Corona Publishing Co., Ltd.: Tokyo, Japan, 1974; pp. 73–115.
24. Ueda, T. *Gas-Liquid Two-Phase Flow [Kieki Nisouryu -Nagare to Netsudentatsu-]*; Yokendo Co., Ltd.: Tokyo, Japan, 1981; pp. 34–51.
25. Akagawa, K. The Flow of the Mixture of Air and Water III. The Friction Losses in Horizontal, Inclined and Vertical Tubes. *Trans. Jpn. Soc. Mech. Eng.* **1957**, *23*, 292–298.
26. Katsuhara, T. Influences of Roughness of Inner Surface of Pipe upon Pressure Drop due to Friction in Two-Phase Flow. *Trans. Jpn. Soc. Mech. Eng.* **1958**, *24*, 1050–1056.
27. Masuyama, T.; Hatakeyama, N. On a Simple Expression of Reynolds Number, and Lower Critical Reynolds Number for Pseudo-Plastic Fluid Flow in Concentric Annular Tubes. *J. MMIJ* **2003**, *119*, 410–415.
28. Masuyama, T.; Hatakeyama, N. On Relation between Friction Factor and Reynolds Number for Pseudo-Plastic Fluid Flow in Concentric Annular Tubes with Roughness. *J. MMIJ* **2006**, *122*, 451–455.
29. Dodge, D.W.; Metzner, A.B. Turbulent Flow of Non-Newtonian Systems. *AIChE J.* **1959**, *5*, 189–204.
30. Metzner, A.B.; Reed, J.C. Flow of Non-Newtonian Fluids—Correlation of the Laminar, Transition, and Turbulent-Flow Regions. *AIChE J.* **1955**, *1*, 434–440.
31. Kemblowski, Z.; Kolodziejski, J. Flow Resistance of Non-Newtonian Fluids in Transitional and Turbulent Flow. *Int. Chem. Eng.* **1973**, *13*, 265–279.
32. Sato, H.; Otsuka, K.; Cui, Y. On theWasp calculation Method -Study of the hydraulic gradient of slurry flow containing mixed size particles. *J. MMIJ* **1988**, *104*, 567–572.
33. Sato, H.; Otsuka, K.; Miyakoshi, H. Terminal Velocity of an Irregular Shaped Particle -Fundamental Studies on Hydraulic Transport of Solids (1st Report). *J. MMIJ* **1978**, *94*, 593–597.
34. API Reference, Discrete Fourier Transform, numpy.fft.fft. Available online: https://numpy.org/doc/stable/reference/generated/numpy.fft.fft.html#numpy.fft.fft (accessed on 27 November 2024).